Lysate-based pipeline to characterize microtubule-associated proteins uncovers unique microtubule behaviours

A. Jijumon, Satish Bodakuntla, Mariya Genova, Mamata Bangera, Violet Sackett, Laetitia Besse, Fatlinda Maksut, Veronique Henriot, Maria Magiera, Minhajuddin Sirajuddin, et al.

Lysate-based pipeline to characterise microtubule-associated proteins uncovers unique microtubule behaviours

A.S. Jijumon[1,2], Satish Bodakuntla[1,2], Mariya Genova[1,2], Mamata Bangera[3], Violet Sackett[1,2,4], Laetitia Besse[5], Fatlinda Maksut[1,2], Veronique Henriot[1,2], Maria M. Magiera[1,2], Minhajuddin Sirajuddin[3] and Carsten Janke[1,2#]

[1]Institut Curie, Université PSL, CNRS UMR3348, F-91401 Orsay, France

[2]Université Paris-Saclay, CNRS UMR3348, F-91401 Orsay, France

[3]Institute for Stem Cell Science and Regenerative Medicine (inStem), Bangalore, India

[4]Department of Ecology and Evolutionary Biology, Brown University, Providence, RI, USA

[5]Institut Curie, Université Paris-Saclay, Centre d'Imagerie Multimodale INSERM US43, CNRS UMS2016, F-91405 Orsay, France

[#]to whom the correspondence should be addressed: Carsten.Janke@curie.fr

Keywords: Microtubules, Microtubule Associated Proteins, Purification-free TIRF assays, microtubule reconstitution, medium-throughput, cell lysate

ABSTRACT

The microtubule (MT) cytoskeleton forms complex macromolecular assemblies with a plethora of MT-associated proteins (MAPs) that play fundamental roles in cell architecture, division and motility. Determining how an individual MAP modulates MT behaviour is an important step in understanding the physiological roles of various MT assemblies. To characterise how the ever-increasing number of MAPs control MT properties and functions, we developed an approach allowing for medium-throughput analyses of MAPs in cell-free conditions using lysates of mammalian cells. Our pipeline allows for quantitative as well as ultrastructural analyses of MT-MAP assemblies. Analysing about fifty *bona-fide* and potential mammalian MAPs, we uncovered previously unknown activities that lead to distinct and unique MT behaviours, such as MT coiling or hook formation, or liquid-liquid phase separation along MT lattice that initiates MT branching. We have thus established a powerful tool for a thorough characterisation of a wide range of MAPs and MAP variants, thus opening avenues for the determination of mechanisms underlying their physiological roles and pathological implications.

MAIN TEXT

Introduction

The microtubule (MT) cytoskeleton is a key structural and mechanical component of all known eukaryotic cells. MTs assemble into a wide variety of dynamic arrays and structures that are implicated in many different cellular functions, such as cell division, motility, shape and intracellular transport. It has been known for decades that building these meta-structures requires distinct sets of microtubule-associated proteins (MAPs), among which are molecular motors[1-3], severing enzymes[4] and proteins that regulate MT plus or minus ends[5]. However, the term "MAP" is usually reserved to describe non-enzymatic proteins that bind to the MT network, which are also referred to as "structural MAPs"[6-8]. While the number of known MAPs is steadily increasing[8] and many novel links to human diseases are being described (Supplementary Table 1 and citations within), most of these proteins remain poorly characterised, thus impeding the understanding of their biological roles.

Characterising MAPs is a non-trivial endeavour. Cell-biological approaches, on one hand, are limited by the fact that the overexpression of MAPs often leads to a variety of artefacts, such as excessive MT bundling. In-depth biochemical and biophysical characterisation, on the other hand, classically employs *in vitro* reconstitution assays that require purification of the MAP in a functional form[9]. Despite recent advances in purifying and studying the role of multiple MAPs, such as MAP7, tau, MAP2, DCX, DCLK1 and MAP9[10], or the role of MAP7 family in controlling kinesin-1[11], such approaches still remain cumbersome and are thus limiting their application to a larger number of MAPs.

Here we established a pipeline to observe a wide variety of MAPs in cell lysates without prior protein purification at single-MT resolution, using total internal reflection fluorescence (TIRF) microscopy. The use of cell lysates was inspired by previous work using *Xenopus laevis* egg extracts to study complex subcellular structures of the cytoskeleton[12, 13], as well as studies employing lysates from yeast[14], or mammalian cells[15-20] to study MT motors and their impact on MT dynamics[21]. Out of the 45 proteins we analysed, some are well-known MAPs, while others inferred to be MAPs based on their colocalisation with MTs in cells, or bioinformatic prediction (Supplementary Table 1). As all proteins were invariably soluble in our lysate approach, we discovered a variety of remarkable, so-far unknown activities by which MAPs affect the behaviour of dynamically growing MTs. We further used our approach to characterise these MT phenotypes in a quantitative manner, and demonstrate that MT-MAP assemblies in lysates allow obtaining MT-binding information by cryo-electron

69 microscopy. Finally, we demonstrate how our method can be used to answer long-standing
70 open questions in the field. Based on an early discovery[22] we reveal that CLIP170, known as a
71 MT-plus-tip binding protein, forms co-condensates of CLIP170 and tubulin at the MT lattice,
72 which can nucleate new MTs, thereby forming branched MTs. Our lysate-based approach is
73 thus a medium-throughput discovery tool that allows screening for properties and functions of
74 MAPs in MT assembly, and can further be extended towards an in-depth characterisation of
75 MAPs and other complex biological assemblies.

76

Results

A lysate-based pipeline for the characterisation MAPs

To enable analyses of any MAP candidate of choice in our pipeline (Fig. 1a), one precondition was to be entirely independent of the availability of pre-existing expression plasmids. Therefore, we based our pipeline on *de-novo* cloning of the open reading frames of proteins of interest using the fast and simple SLIC[23] approach (Step 1, Extended Data Fig. 1). All *bona-fide* and potential MAPs were fused to the fluorescent protein at the carboxy-terminus, except MAPs that had been analysed before, where we followed the tag positioning found in the literature (Supplementary Table 1).

The expression of fluorescently-tagged proteins was first tested in U-2 OS cells, allowing to verify the intracellular localisation of the proteins (option to step 2, Fig 1a; Fig. 2a; Extended Data Fig. 2; Supplementary information Fig. 1). For cell-free assays, GFP-tagged MAPs (GFP-MAPs) were expressed in HEK-293 cells (Step 2, Fig 1a), from which soluble cytosolic lysates containing the overexpressed, fluorescently-tagged proteins were generated (Step 3, Fig 1a). Controlling total protein concentrations in all lysates assured similar concentrations of endogenous tubulin in all assays, as tubulin concentrations in cells are strictly regulated in cells[24-26]. Therefore, observed differences in the MT growth behaviour in our assays can be directly attributed to the effect of the GFP-MAPs, which are the sole variable component. Cell lysates were directly introduced into flow chambers where MT polymerisation was recorded by TIRF microscopy (Step 4, Fig 1a). The impact of MAPs on dynamic MTs was observed by recording the GFP-MAPs; MTs and F-actin were visualised by post-staining. Cell lysates were also directly used in ultrastructural studies using cryo-electron microscopy (option to Step 4, Fig 1a).

We validated our assay with two well-characterised MT-interacting proteins: the MT-severing enzyme spastin and the end-binding protein 3 (EB3). Purified spastin is known to efficiently sever MTs[27]. When we incubated taxol-stabilised MTs with lysates of spastin-expressing cells, we observed efficient MT severing (Fig. 1b; Supplementary Video 1a). EB3, which tracks growing MT plus ends[28], also did so in lysates (Fig. 1c; Supplementary Video 1b). This demonstrates that our lysate-based approach faithfully reproduces MT-MAP interactions that are known from previous cell-based or *in-vitro* reconstitution assays.

Systematic characterisation of 45 *bona-fide* or candidate MAPs

We next selected a representative panel of 45 *bona-fide*, or candidate MAPs from the literature (Supplementary Table 1). Expression of these 45 proteins in U-2 OS cells (Extended Data Fig. 2; Supplementary information Fig. 1) revealed three principal phenotypes: MAPs that (i) strongly bundle MTs, (ii) decorate MTs and rarely induce visible MT bundles, or (iii) show no MT binding at all (Fig. 2a). We observed some variations within these categories, for instance, among MAPs that bundle MTs some generated thick MT bundles (e.g. Tau, MAP2), while others formed thinner and wavy MT bundles (e.g. GLFND1, MAP7D3). Despite these variations, it was straight-forward to distinguish MT bundling and categorise all MAPs (Fig. 2c; Extended Data Fig. 2; Supplementary information Fig. 1).

We next prepared lysates of HEK 293 cells expressing the selected 45 MAPs or MAP candidates and recorded their impact on dynamically growing MTs by TIRF microscopy. We performed at least three independent assays to ensure the reproducibility of our observations. 40 out of the 45 tested proteins co-localised with growing MTs in lysates (Fig. 2b, Extended Data Fig. 3-6; Supplementary information Fig. 2; Supplementary Videos 2-13). Most MAPs also induced MT polymerisation independently from the MT seeds (Fig. 2c, grey squares). In some cases, it was difficult to determine whether the newly polymerised MTs were assembled from the seeds (Fig. 2c, grey half-squares). For MAPs with strong nucleation activities, we observed much higher MT densities as compared to control, or lysates expressing MAP candidates that did not bind MTs. This indicates that de-novo MT nucleation and assembly might be a general characteristic of many MAPs than those previously reported[29, 30].

Labelling of MTs and actin by post-staining revealed that 11 MAPs strongly increased the co-localisation of actin filaments (F-actin) with MTs (Fig. 2c, full red squares), suggesting that they promote alignment of F-actin with MTs. To determine the potential role of such MT-actin interactions in MT behaviour, we prevented actin polymerisation with Latrunculin A[31, 32]. Absence of actin polymerisation in our assays did not impede any MAPs to associate with MTs, nor did it fundamentally change the appearance of the MT networks (Extended Data Fig. 3-6; Supplementary information Fig. 2; Supplementary Videos 2-13). This suggests that the co-alignment of F-actin to MTs by some of the here-tested MAPs has no essential role in the formation of MT arrays by these MAPs.

Based on our observations we categorised the 45 candidate MAPs into (i) MAPs that bind MTs, but do not align with F-actin, (ii) MAPs that bind MTs and promote co-alignment of F-actin and MTs, and (iii) proteins that do not bind MTs (Fig. 2b). A combined, schematic representation of MAP behaviour in cells and the lysate-based experiments (Fig. 2c) shows

that most MAPs associating with MTs in cells also promote polymerisation and growth of MTs in lysates. This confirms our pipeline as a powerful and versatile tool to analyse the impact of MT-interacting proteins on growing MTs in cell-free conditions.

The impact of individual MAP-family members on MT behaviour

One of the advantages of our pipeline lies in the opportunity to compare side-by-side MAPs that have previously been characterised only in isolated studies. When comparing members of the mammalian EMAP-like protein (EML) family in our assay, we discovered striking differences in their behaviour. While EML1, 3 and 4 associated with growing MTs, no MT polymerisation was observed in the presence of EML2 (Extended Data Fig. 4; Supplementary Video 5), confirming a previous observation that EML2 (also known as EMAP-like protein 70) exhibits MT depolymerising activity[33]. Among EMLs that bound MTs, EML1 and EML4 strongly associated with growing MTs, while EML3 accumulated with a delay at apparently pre-existing MTs (Extended Data Fig. 4; Supplementary Video 5). Finally, EML1 showed a unique feature of accumulation towards growing MT ends. This, however, was visible only at early time points of MT growth but later obscured by uniform accumulation of EML1-GFP all-along MTs (Extended Data Fig. 4a; Supplementary Video 5a). We thus demonstrated that despite their sequence similarity, each of the EML proteins has a distinct type of MT interaction.

The MAP7 family comprises four different proteins: MAP7, MAP7D1, MAP7D2 and MAP7D3[34-36], which were shown to participate to different degrees in linking kinesin to MTs in a thorough *in-vitro* study[11]. In our lysate approach, MAP7, but none of the other MAP7 family members, induced the formation of characteristic aster-like MT arrays (Extended Data Fig. 5; Fig. 3a,b; Supplementary Videos 9,14). This observation is coherent with the function of MAP7 as a mediator of kinesin-MT interactions[11, 37], and suggests that MAP7 recruits endogenous kinesin motors from the cell lysates, thereby inducing aster formation[38]. What was striking was not the mere fact that MAP7 induced aster formation, but that none of the other 44 MAPs tested here did so. This unique feature could either reflect the way MAP7 binds to MTs in conjunction with kinesin motors, or by recruitment of additional cofactors from the cell lysate that participate in the formation of these unique MT arrays. These findings might therefore provide a framework for deeper mechanistic characterisation of MAP7-induced formation of MT asters.

Discovery of unique MT behaviours induced by MAPs

Some MAPs analysed here showed unique, previously undescribed features with growing MTs in lysates. The centriole, cilia and spindle-associated protein (CSAP), first reported as a MAP specifically colocalising with polyglutamylated MTs on centrioles, mitotic spindles, and cilia[39], and later as a recruitment factor of polyglutamylating enzymes to MTs[40], induced the formation of MT helices in lysates (Fig. 3a,b; Extended Data Fig. 3b; Supplementary Videos 3d,14). To visualise these MT coils, we used the HILO imaging mode, which allows a higher penetration depth than the TIRF mode[41]. We measured ~40 CSAP-induced MT coils (Extended Data Fig. 7a) and found a helix width of ~900 nm (Fig. 3c). A similar MT phenotype had so far only been reported for MAP6/STOP[42].

Strikingly, the discovery of previously unknown activities of MAPs in cell lysates was not restricted to scantily studied MAPs such as CSAP. We also discovered a previously undescribed activity for the well-characterised MT-actin crosslinker MACF1[43-45]. Because of the large size of MACF1 (~600 kDa), and our focus on MT binders, we used a truncated version of the protein encoding the carboxy-terminal 1023 amino acids (amino acid 4305-end) that include the MT-binding domain[45], called MACF1_C1023. In lysates, MACF1_C1023-GFP decorates the lattice of growing MTs, which spontaneously formed hooks at their growing ends that prevented further MT elongation (Fig. 3a,b; Extended Data Fig. 3c; Supplementary Videos 7b,14). Measuring >100 individual hooks (Extended Data Fig. 7b) revealed an average diameter of ~1.02 ± 0.15 µm (Fig. 3d). This phenotype appears to be specific to MACF1, as the homologue MACF2 (dystonin) did not form similar structures in our assays (Extended Data Fig. 3d; Supplementary Video 7c).

MAP2, a neuronal MAP[46] expressed either as high-molecular-weight splice isoforms MAP2A and MAP2B (~280 kDa)[47], or as smaller isoforms MAP2C (~51 kDa) and MAP2D (~54 kDa)[48, 49] strongly promotes MT polymerisation in lysates (Extended Data Fig. 6a,b; Supplementary Videos 7d,8a). Here we observed a previously unknown activity of MAP2C and MAP2D, the induction of faint, hook-like structures that might be transitionary deformations of either whole MT lattice, or of a subset of protofilaments. These structures initiate the accumulation of MAP2 into small clusters, or droplet-like assemblies (Fig. 3a,b; Supplementary Video 14). The increase of GFP fluorescence intensity over time showed that these clusters progressively accumulate MAP2. In some cases, MAP2 clusters terminated MT

growth (Extended Data Fig. 7c). Our observation that this phenotype was more pronounced for MAP2D as compared to MAP2C (Extended Data Fig. 6a,b; Supplementary Videos 7d,8a) suggests that it directly depends on the interaction strength between MAP2 and MTs, which is stronger for MAP2D due to the presence of an additional MT-binding tandem repeat in this isoform[48]. Strikingly, a similar cluster formation was not observed with the highly similar Tau protein (Extended Data Fig. 6c,d; Supplementary Video 12c,d).

Finally, we observed that MTs in lysates were gliding when decorated with DCLK, DCX, MAP2, MAP8, MAP11 and Tau (Supplementary Videos 4,7d,8a,10a,b,12c,d), and to a lesser extent with CKAP2, CKAP2L, EML1 and MAP9 (Supplementary Videos 3b,c,5a,10b). MT gliding activity could occur when a MAP bound to an attached MT captures a motor protein from the cell lysate in a way that activates the motor domain, which in turn would move unattached MTs in the lysate. Uncovering this active motor component could reveal other motor regulatory mechanisms by MAPs, which could be fundamentally different from the way MAP7 is recruiting kinesin[11].

Determining the impact of MAP concentrations in lysates

The capacity of MAPs to control MT assembly and dynamics, and their ability to induce the formation of specific MT arrays is concentration-dependent[50-54]. To determine the impact of MAP concentrations in lysates, we investigated the formation of MT hooks by MACF1_C1023 (Fig. 3a,b; Supplementary Video 14). We estimated the concentration of MACF1_C1023-GFP in the lysate to be 520 nM by immunoblot (Fig. 4a). By performing dilutions with lysate from non-transfected cells, we then prepared lysates in which the concentration of MACF1_C1023-GFP was decreased, while the overall protein concentration of the lysates was maintained at 8 mg/ml. In lysates containing 520 nM MACF1_C1023-GFP, MT growth was rapidly stalled by hook formation, whereas at 260 nM, MTs grew more persistently before forming hooks. At 130 nM, the number of MTs forming hooks was strongly decreased, and no MT hooks at all were formed at 65 nM MACF1_C1023-GFP (Fig. 4b; Supplementary Video 15). The concentration dependency of MACF1-induced MT hook formation suggests that in cells, MT hooks might be induced by local accumulation of MACF1.

Determining the impact of disease-related mutations of MAPs

Whole-genome or exome sequencing of patients with genetic diseases reveals a growing number of MAPs with mutations linked to a spectrum of human disorders (Supplementary Table 1). Being able to rapidly and reliably test the impact of these mutations on the functions of MAPs is essential for the understanding of the molecular mechanisms underlying these diseases. To test whether our lysate-based approach could be used for the functional characterisation of MAP mutations, we analysed an EML1 mutation (EML1^{Thr243Ala}) from patients with subcortical heterotopia, a neurodevelopmental disorder leading to brain malformation[55, 56]. To directly compare mutant and wild-type proteins, we mixed lysates from cells expressing wild-type EML1-GFP and EML1^{Thr243Ala}-mCherry 1:1 and concomitantly observed the behaviour of both proteins during MT polymerisation (Fig. 5a). While the EML1-GFP strongly decorated the rapidly polymerising MTs, EML1^{Thr243Ala}-mCherry showed no MT decoration (Fig. 5b; Supplementary Video 16a). Experiments with swapped fluorescent tags, i.e. wild-type EML1-mCherry and EML1^{Thr243Ala}-GFP, yielded the same result, thus excluding a potential impact of the fluorescent protein tags (Extended Data Fig. 8; Supplementary Video 16b). This demonstrates that the Thr243Ala mutation of EML1 leads to a strong decrease of its MT-binding capacity, which in turn might affect the overall dynamics and architecture of the MT cytoskeleton in the neurons of patients carrying this mutation[55, 56].

Apart from a high throughput that allows concomitant screening of a panel of mutations, our lysate-based approach has the capacity to reveal indirect effects of mutations, such as causing the sequestration of a MAP, or a MAP becoming less competitive for binding to a site shared with another MT binder that is likely to be present in the cell lysate. Such indirect effects would not be detected in *in-vitro* binding assays with purified components. This makes our pipeline a promising tool for the medium- to large-scale analyses of disease-related MAP mutations.

Ultrastructural studies of MAP-MT assemblies in cell lysates

One of the greatest challenges to understand MT-MAP interactions at the structural level is that many MAPs are intrinsically unstructured proteins. Recent advances in cryo-electron microscopy have demonstrated that MAPs can adapt defined structures upon their binding to the MT surface, and delivered detailed insight into their mode of binding[57-60]. Similar to *in-vitro* reconstitution experiments, structural studies require purified, functional MAPs, thus encountering the known limitations of protein purification. Having demonstrated that virtually all MAPs characterised here were soluble and functional in cell lysates, we tested whether

high-resolution structures of MAPs decorating MTs can be obtained from cell lysates, which had so far only been done for membrane-bound proteins[61].

We first adapted our pipeline to cryo-EM requirements. Pre-polymerised GMPCPP-MT seeds were attached to EM grids mounted to the Vitrobot, incubated with cell lysates to allow MT polymerisation, plunge-frozen and imaged (Fig. 6a). Additional tubulin was added to MACF1_C1023-GFP lysates to allow the formation of the MACF1_C1023-induced MT structures within the 2-min time constraint of the freezing approach, as the characteristic MT hooks induced by MACF1_C1023 were mostly observed between 5-10 min by TIRF microscopy (Fig. 3; Supplementary Video 14). Electron micrographs from GMPCPP-MTs assembled from pure tubulin showed an undecorated MT structure; by contrast, MTs assembled in the presence of EML1, EML4 and MACF1_C1023 in lysates showed a regular MT decoration in the micrographs (Fig. 6b). Moreover, while EML1 and EML4 generated straight MTs, MTs formed with MACF1_C1023 showed splayed ends, as well as structures resembling protofilament rings (Fig. 6b). It is possible that the splayed MT ends are precursors for the formation of MT hooks (Fig. 3; Supplementary Video 14).

We next performed a helical reconstruction of MTs decorated with full-length EML1, and obtained a high-resolution structure showing densities of EML1 bound along a 14-protofilament MT. The MT part of the reconstruction was resolved to 3.7 Å, while the resolution of the electron density corresponding to EML1 was considerably lower. The pattern of decoration resembled a previously determined structure of a 207-amino-acid amino-terminal fragment of EML4 (EML4_N207), obtained with MTs assembled from purified brain tubulin and recombinant EML4_N207[58] (Fig. 6c; Supplementary Video 17). To directly compare the MT binding modes of both proteins, we fitted EML1 and EML4_N207 densities with models for α- and β-tubulin. The overlay images revealed that both proteins bind similarly to the ridges of the protofilaments, where they might interact with flexible carboxy-terminal tubulin tails that were not resolved (Fig. 6d).

Our lysate-based approach thus permits the acquisition of electron density maps of MAPs bound to MTs at high resolution, which can be used for reconstruction of high-resolution structures revealing binding modes of MAPs to MTs. The lower resolution of the MAP as compared to the MTs could originate from the higher flexibility of these proteins, in which case the same limitations would be found with purified proteins. Alternatively, lower resolution of a MAP could be caused by sub-stochiometric binding to the MT lattice. This can be easily overcome with purified components by increasing the MAP concentration, but

would require the optimisation of the expression conditions of MAPs in cells to increase their concentrations in the cell lysates. Nevertheless, even low-resolution images of MAPs for which no other structural data are available could provide important information about the mode of binding, and whether competition with other MT interactors could occur.

Droplet formation by CLIP170 along MTs in lysates

Having discovered previously unknown activities for well-characterised MAPs, such as MACF1, MAP2 and MAP7 encouraged us to revisit CLIP170, a protein with extensively characterised MT +TIP-tracking properties[62-65]. Intriguingly, however, early observations had shown that CLIP170 can also form patches in cells[22], reminiscent of liquid-liquid phase separation, which was confirmed by a recent study[66].

Live-imaging of overexpressed GFP-CLIP170 in U-2 OS cells showed the formation of dynamic GFP patches that emanate from small droplets, which coalesce and deform over time, typical for liquid-like behaviour[66, 67] (Fig. 7a; Supplementary Video 18a). CLIP170 droplets and patches in cells appeared to line MTs and MT bundles (Fig. 7b), suggesting that droplet formation is MT-mediated. We thus examined CLIP170 behaviour in cell lysates, where it indeed formed chains of droplets along MTs. The fluorescence intensity of these droplets (Fig. 7c; Supplementary Video 18b), as well as their diameter (Fig. 7d) increased over time, indicating a progressive accumulation of CLIP170. In some instances, droplets coalesced, which was revealed by an increasing median distance between maximum-fluorescence peaks over time (Fig. 7e).

To determine the concentration-dependency of CLIP170-droplet formation, we prepared a series of lysates with decreasing CLIP170, but constant overall protein concentrations. Reduced CLIP170 concentrations led to the formation of smaller droplets (Fig. 7f,g). Intriguingly, not just the size, but also the spacing of the droplets decreased (Fig. 7h; Extended Data Fig. 9), indicating a topological link between these two parameters. We further tested the behaviour of these droplets in the presence of 1,6-hexanediol, known to dissolve protein condensates that are formed by hydrophobic interactions, as it had been shown for condensates of tau on MTs[68]. Our observation that CLIP170 patches were not dissolved by 1,6-hexanediol (Extended Data Fig. 10, Supplementary Video 19) indicates that their formation might not result from hydrophobic interactions[67].

Liquid-like droplets of another MT-interacting protein, TPX2, have recently been demonstrated to induce the formation of branched MT networks[69]. To determine whether CLIP170 droplets have a similar activity, we first allowed the formation of MTs decorated with CLIP170 droplets, followed by a second step in which the droplet-decorated MTs were incubated with fresh lysate lacking CLIP170 (Fig. 8a). To visualise MTs in these experiments, lysates where prepared from HeLa Kyoto cells expressing mCherry-α-tubulin[70]. During the initial assembly of CLIP170-decorated MTs, mCherry-α-tubulin accumulated in the CLIP170 droplets (Fig. 8b). After lysate exchange, we observed de-novo polymerisation of MTs that almost exclusively originated from CLIP170 droplets (Fig. 8c; Supplementary Video 18c), which was further underpinned by post-staining of MTs (Fig. 8d). This suggests an active role of CLIP170 in the initiation of MT assembly on existing MTs, and thus in the formation of MT branches.

Discussion

The MT cytoskeleton is an interaction hub for a multitude of proteins. Understanding how MT-interacting proteins control the properties and functions of MTs is essential for deciphering the working of the MT cytoskeleton. While *in vitro* reconstitution assays of MT arrays from purified components are a gold standard[9], they critically depend on the successful purification of functional components, which is often a major stumbling stone. As a consequence, only some proteins could so far be thoroughly characterised, which in the light of the constantly growing list of newly discovered MT interactors impedes advances towards a holistic understanding of MT architecture and functions. Moreover, the growing number of links between MAPs and human disorders (Supplementary Table 1)[8] makes it primordial to establish approaches that allow faster and less constrained characterisation of MAP-MT assemblies in cell-free settings.

We demonstrate here that using lysates from mammalian cells overexpressing fluorescently labelled proteins allows to circumvent the most daunting bottleneck of reconstitution assays; the purification of novel proteins. In a set of 45 *bona-fide* or candidate MAPs (Supplementary Table 1), all proteins remained soluble in cell lysates, which allowed a systematic, comparative characterisation of their interactions with individual, dynamically growing MTs (Fig. 2). The fact that all components needed for MT polymerisation, i.e. free tubulin and GTP, come directly from the cell lysates, makes the assay highly reproducible and

independent from additional factors, such as the quality of purified tubulin used in classical *in-vitro* reconstitutions. Strikingly, many of the MT-MAP assemblies we observed in assays with cell lysates were not seen on MTs inside cells overexpressing the same MAPs, most likely due to spatial constraints inside the cells, or to the propensity of most MAPs to induce MT bundling. This underpins the unique capacity of the assay to discover previously unknown MAP activities.

In contrast to *in vitro* reconstitutions with purified components, lysates cannot be used to determine the minimal set of components needed to build macromolecular assemblies. The presence of cellular proteins in the lysates, however, provides the great opportunity to identify protein complexes interacting with MTs that would never have been discovered by conventional biochemical methods. MTs with associated MAPs and their unknown interactors could be purified and identified by proteomics. To increase the specificity of this approach, proximity-ligation approaches such as bio-ID[71] followed by purification and identification of biotinylated proteins could be employed.

A potential limitation of our method is that MAPs concentrations in lysates are in limited by efficiency of their expression, which could for instance limit the resolution of MAP in structural studies. For most proteins, this could be overcome by increasing the amount of plasmid transfected into the cells, and/or by increasing expression time. Of the 45 proteins tested here, low expression levels were rather rare, and surprisingly little related to the overall size of the overexpressed proteins. For proteins that are particularly hard to express, additional steps such as changing the position of the fluorescent tag, or optimising the coding sequence to avoid rare codons or the formation of mRNA secondary structures that hinder ribosome progression[72] could be employed.

While determining concentration of MAPs is more difficult in lysates as compared to purified proteins, this does not impede a quantitative evaluation of the concentration-dependency of MAP-induced MT phenotypes, as we demonstrated here for MACF1_C1023 and CLIP170. Whether the concentrations we found to induce specific MT structures correspond to the average intracellular concentration of a particular MAP is not necessarily relevant, given that many MAPs can be locally enriched in cells. MACF1, for instance, might be targeted via its amino-terminal actin-binding domain specifically to actin-rich subcellular compartments such as the leading edge or the neuronal growth cone[73], and form MT hooks only at those locations. The MT phenotypes we have described here might thus represent rare, locally restricted MT structures in cells, which have so-far been overlooked. However, they might

play important roles in the formation of specific MT meta-structures, and their initial demonstration in lysates becomes an essential prerequisite for the characterisation of their cellular functions.

We thus established and validated a reconstitution assay of cytoskeletal assemblies in cell lysates as a fast, straightforward and medium-throughput approach to characterise MAP-MT assemblies at single-MT resolution. Our success in obtaining persistently soluble and functional full-length proteins illustrates the power of this method. By demonstrating the suitability of our assay for reproducible quantitative measurements, ultrastructural analyses, and its capacity to be extended to study cytoskeletal crosstalk and to characterise disease-related mutations, we illustrate how our pipeline can transform research on cytoskeletal mechanisms and their impact on a wide variety of cellular functions and human diseases.

ACKNOWLEDGEMENTS

This work was supported by the ANR-10-IDEX-0001-02, the LabEx Cell'n'Scale ANR-11-LBX-0038 and the Institut de convergence Q-life ANR-17-CONV-0005. CJ is supported by the Institut Curie, the French National Research Agency (ANR) awards ANR-12-BSV2-0007 and ANR-17-CE13-0021, the Institut National du Cancer (INCA) grant 2014-PL BIO-11-ICR-1, and the Fondation pour la Recherche Medicale (FRM) grant DEQ20170336756. JAS was supported by the European Union's Horizon 2020 research and innovation programme under the Marie Skłodowska-Curie grant agreement No 675737, and the FRM grant FDT201904008210. SB was supported by the FRM grant FDT201805005465. MS acknowledges funding support from DBT/Wellcome Trust India Alliance Intermediate Fellowship (IA/I/14/2/501533), EMBO Young Investigator Programme award, CEFIPRA (5703-1), Department of Science and Technology, SERB-EMR grant (CRG/2019/003246) and DBT-BIRAC (BT/PR40389/COT/142/6/2020). The authors acknowledge the National CryoEM Facility at Bangalore Life Science Cluster, Bangalore, India and the funding by B-life grant from Department of Biotechnology (DBT/PR12422/MED/31/287/2014). The authors acknowledge the National CryoEM Facility at Bangalore Life Science Cluster and funding by B-life grant from Department of Biotechnology (DBT/PR12422/MED/31/287/2014).

MMM is supported by the Fondation Vaincre Alzheimer grant FR-16055p.

We thank the team of T. Surrey (Francis Crick Institute, London) for technical advice and training, L. Kainka, F. Lautenschläger, G. M. Montalvo Bereau (Universität des Saarlandes, Saarbrücken, Germany) for experimental support. We also thank S. Citi (University of Geneva, Switzerland), F. Francis (Inserm, Paris, France), D. Gerlich (IMBA Vienna, Austria), N. Manel (Institut Curie Paris, France), C. Nahmias (Gustave Roussy Cancer Center, Villjuif, France) for providing essential reagents, as well as C. Messaoudi, M.-N. Soler and C. Lovo from the Multimodal Imaging Center (MIC; CNRS UMR2016 / Inserm US43) for support with imaging and image analyses. We are grateful to T. Müller-Reichert (Technical University Dresden, Germany), P. Tran (Institut Curie, Paris, France) for insightful discussions and advice.

AUTHOR CONTRIBUTIONS STATEMENT

JAS established the lysate-based pipeline and performed all experiments related to it. Lysate experiments shown in Extended Data Fig. 10 and Supplementary Video 19 were performed by MG. SB, FM and VH performed molecular cloning and sequence analyses with the help of JAS and MG. SB performed all cell biology experiments. SB and VS performed cell live imaging experiments. MG purified proteins and established quantitative approaches with JAS. MB performed electron microscopy studies and analyses. JAS and LB analysed and quantified imaging data with the help of SB. JAS, SB and CJ analysed data and prepared figures and videos with the help of MB and LB. MS supervised electron microscopy studies and analyses. CJ supervised the study with the help of MMM. JAS, SB, MMM, MS and CJ acquired funding. JAS, SB and CJ wrote the manuscript with the help of MG, MB, MMM and MS.

COMPETING INTERESTS STATEMENT

The authors declare no competing interests.

FIGURE LEGENDS

Figure 1: A pipeline to analyse MAP-MT assemblies in cell lysates

a) Schematic representation of the pipeline used in this study. In step 1, MAPs of interest are amplified from different cDNA libraries, cloned into expression plasmids, and sequenced. In some cases, different isoforms are identified. In step 2, fluorescently labelled MAPs are expressed in HEK 293 cells for cell lysates, and in U-2 OS cells to determine their intracellular behaviour. In step 3, HEK 293 cells are lysed, and clarified lysates are used in step 4 to perform TIRF assays assembling MTs in the presence of fluorescent MAPs in the lysates. Optionally, GFP-MAP concentrations in lysates can be quantified, and MAP-decorated MTs can be used in cryo-electron microscopy.

b) Spastin-GFP from cell lysates severs taxol-stabilised MTs. Zoom images highlight the progressive fragmentation of a MT. N = 4 independent TIRF assays conducted using 3 independent cell lysate preparations.

c) EB3-GFP from cell lysates tracks growing MT ends. Zoom images highlight the enrichment of EB3-GFP (white arrow heads) at a growing MT tip. N = 5 independent TIRF assays conducted using 4 independent cell lysate preparations.

Numerical data are available in source data.

Figure 2: Systematic characterisation of 45 MAP candidates

a) GFP-tagged MAPs, or presumed MAPs, expressed in U-2 OS cells show three principal behaviours in cells: strong MT bundling, MT decoration with rare formation of bundles, or no obvious MT binding. Three representative proteins, co-labelled with anti-α-tubulin antibody to visualise MTs, are shown (see Extended Data Fig. 2; Supplementary information Fig. 1 for all 45 proteins analysed). MT bundles are defined as thick fibres that are labelled much stronger with anti-α-tubulin antibody than MTs in control cells. In all observed cases, they co-localise with the overexpressed GFP-MAP. N = 19 cells (Tau-0N-04R), n = 36 cells (MAP9-GFP) and n = 106 cells (MAP11-GFP) from two independent experiments.

b) GFP-tagged MAPs in lysates observed by TIRF microscopy decorate growing MTs. At the end of the time-lapse imaging (12 min), MTs and actin are visualised with YL1/2 antibody and SiR-actin to determine whether a MAP aligns spontaneously forming actin fibres (F-actin) to the MTs in the lysate. Some presumed MAPs did not decorate MTs in lysates. Three

representative examples from 45 proteins are shown (other examples are shown in Extended Data Fig. 3-6; all 45 proteins are shown in the Supplementary information Fig. 2 and Supplementary videos 2-13). N = 14 (MACF1_C1023), n = 4 (DCX) and n = 3 (JPL1) independent TIRF assays from 7, 3 and 2 independent cell lysates.

c) Summary of the behaviour of 45 proteins in cells (Extended Data Fig. 2; Supplementary information Fig. 1) and in cell lysates (Extended Data Fig. 3-6; Supplementary information Fig. 2; Supplementary Videos 2-13). Grey bars show relative size of proteins, number of amino acids, and the position of the GFP tag (green). Truncated MAPs are indicated. Classification of MAP behaviours uses same colour codes as in (a) and (b). MAPs showing partial, or weak characteristics are visualised by half-squares. MT nucleation was evaluated within the initial 5 min of the experiments. Full squares indicate MAPs leading to massive spontaneous MT nucleation. Half-squares indicate no clearly discernible spontaneous MT nucleation, with most MTs growing from seeds, and only few MTs without visible seed entered the field of observation. Details of the experimental repeats of 45 proteins are provided as source data.

Figure 3: Discovery of unique activities of MAPs on growing MTs

a) Representative time-lapse images of selected MAPs inducing unique MT behaviour in lysates. MAPs are false-colour-coded (see Supplementary Video 14). Arrowheads indicate growing CSAP-induced MT coils. **b)** Zoom images and schematics showing the typical behaviour induced by the respective MAPs. Tubulin labelling with YL1/2 antibody is shown in white. Growth directions of the MTs are indicated by arrows. All MT phenotypes were observed in at least 3 independent TIRF assays from at least 3 sets of independent lysate preparations. Numerical data for each MT phenotype is available in source data. **c)** Determination of the average width of CSAP-induced MT coils. Quantification of about 40 coils (Extended Data Fig. 7a) showed an average width of about 900 nm. Data are presented as scatter plots with mean ± SD. Quantification was performed from n = 4 independent TIRF assays using 3 independent cell lysate preparations. **d)** Quantification of the diameter of MT hooks induced by MACF1_C1023. Measurements of over 100 MT hooks (Extended Data Fig. 7b) from n = 5 independent TIRF assays using 4 independent cell extracts showed an average hook diameter of about 1 µm. Data are presented as scatter plots with mean ± standard deviation (SD). Numerical data for (c) and (d) are available in source data.

Figure 4: Determining the impact of MAP-GFP concentrations on MT behaviour in lysates

a) Determination of the concentration of MACF1_C1023-GFP by quantitative immunoblot. Purified GFP with known concentrations was analysed by immunoblot together with different dilutions of the lysate from HEK 293 cells expressing MACF1_C1023-GFP. The intensities of the bands labelled with anti-GFP antibody was determined, and plotted against the known concentrations of the purified GFP dilution series. The plot shows the linearity of the calibration curve. The three values determined from different dilutions of the MACF1_C1023-GFP lysates were used to determine the concentration of the protein in each sample. The values were then concentration-adjusted and averaged to determine the final concentration of MACF1_C1023-GFP, which was found to be 520 nM in the undiluted lysate. Immunoblotting of MACF1_C1023-GFP quantification was performed once.

b) The impact of MACF1_C1023-GFP concentration on MT hook formation (red arrowheads) was determined in lysates with four defined concentrations of this MAP. Time lapse images of MACF1_C1023-GFP (GFP shown in inverted grey scale) show that hook formation propensity decreases relative to the number of MTs with decreasing MACF1_C1023-GFP concentrations (see Supplementary Video 15). $N \leq 2$ independent TIRF assays for each concentration from one set of cell lysate having quantified MACF1_C1023-GFP concentration (a).

Numerical data and unprocessed gels and immunoblots are available in source data.

Figure 5: The impact of a disease-related mutation of EML1 on MT binding

a) Schematic representation of the work flow. GFP-MAP encoding plasmids are mutagenized to introduce a disease related mutation, and fluorescent tags are swapped to obtain a GFP and an mCherry version of both, wild-type and mutant MAP. Cell extracts are prepared for each expression construct separately, and cell lysates are mixed before TIRF assays.

b) Still images from time-lapse (Supplementary Videos 16a) of MTs polymerising in a 1:1 mixture of lysates from HEK 293 cells expressing wild-type EML1-GFP and EML1^{Thr243Ala}-mCherry. MT seeds are visualised in the red channel together with EML1^{Thr243Ala}-mCherry. Note that EML1-GFP strongly decorates polymerising MTs, while no MT labelling was

552 detected for EML1^{Thr243Ala}-mCherry. N = 4 independent TIRF assays from 3 sets of
553 independent cell lysate preparation. This result was confirmed with EML1-mCherry and
554 EML1^{Thr243Ala}-GFP (Extended Data Fig. 8; Supplementary Videos 16b).

555

556 **Figure 6: Structural analyses of MAP-MT assemblies in lysates using cryo-electron**
557 **microscopy**

558 **a)** Flow diagram of the pipeline for cryo-electron microscopy (cryo-EM) using MAP-
559 containing lysates. Lysates were initially tested and optimised to show the previously
560 observed MT phenotypes (Extended Data Fig. 3,4) by TIRF microscopy. Lysates were then
561 added onto EM grids with GMPCPP-MT seeds. After 20-120 s incubation, grids were plunge-
562 frozen in liquid ethane, transferred to an electron microscope, and acquired images were
563 processed to obtain 3D reconstructions.

564 **b)** 2D cryo-electron micrographs and false-coloured zoom images of individual MTs in
565 absence of MAPs stabilised with GMPCPP, or in presence of EML1-GFP, EML4-GFP, and
566 MACF1_C1023-GFP. MTs were polymerised from endogenous tubulin in the lysates
567 (additional tubulin was added to MACF1_C1023-GFP lysates). Black arrows show MT-
568 associated densities, blue arrows highlight tubulin ring formations, and crimson arrows show
569 protofilaments about to peel off in the presence of MACF1_C1023-GFP.

570 **c)** Top and lateral views of a symmetrised helical reconstruction (resolution 3.7 Å, low-pass
571 filtered to 15 Å) of 14-protofilament MTs (grey) with extra densities corresponding to EML1-
572 GFP (green). Comparison with a similar helical reconstruction (EMDB 1331; resolution
573 3.6 Å, low-pass filtered to 15 Å) obtained for 13-protofilament MTs (polymerised from brain
574 tubulin) with purified EML4_207 (red)[58]. Note that both MAPs bind along the MT
575 protofilament ridge (see Supplementary Video 17). In total, 1143 micrographs were used for
576 the helical reconstructions of MT decorated with EML1-GFP. Three unprocessed images are
577 shown in Supplementary information Fig. 3.

578 **d)** Densities for a single protofilaments from the symmetrised reconstruction low-pass filtered
579 to 15 Å. The fitted models for α- and β-tubulin (PDB ID 6dpu for EML1-GFP; PDB ID 6i2i
580 for EML4_N207) are shown in light and dark grey as mesh, respectively. The position of
581 associated extra densities corresponding to EML1-GFP (green) and EML4_N207 (red)
582 suggests interactions of the proteins with the flexible carboxy-terminal tails. These tails are
583 not resolved, however their origin at the end of helix 12 is indicated. A superposition of the

electron density maps of EML1-GFP and EML4_N207 shows that both MAPs bind at similar positions of the tubulin molecules within the MTs.

Numerical data are available in source data.

Figure 7: Characterisation of droplet formation by CLIP170

a) Time series from a video showing accumulation of overexpressed GFP-CLIP170 in a U-2 OS cell. Cell contours were visualised by bright-field microscopy. Note that initially formed small droplets were later fusing, and GFP patches deform over time (Supplementary Video 18a). N = 24 cells from 2 independent experiments.

b) U-2 OS cell stained with anti-tubulin antibody show formation of chains of small GFP-CLIP170 droplets along bundled MTs, or bigger patches mostly lined up with MTs. N = 40 cells from 4 independent experiments.

c) Time-lapse of lysates with GFP-CLIP170 (white). GFP-CLIP170 formed regularly spaced droplets along the MTs. Droplet intensity along one MT (orange line) is plotted below (see Supplementary Video 18b). N = 12 independent TIRF assays from 8 independent cell lysate preparations.

d) Droplet diameters from each time frame shown in (c). Note that the droplet size increases over time. N = 9 - 57 GFP-CLIP170 droplets from each time point from a representative experiment (c) were used. Data are presented as scatter plots with median with 95% confidence interval (CI). Significance was tested using one-way ANOVA followed by Tukey's multiple comparisons test.

e) Droplet distances were measured as distances between local maxima in intensity profiles (c). Increase of droplet distances over time indicates droplets fusion. N = 17- 48 GFP-CLIP170 droplets from each time point from a representative experiment (c). Data are presented as scatter plots with median with 95% confidence interval (CI). Significance was tested using one-way ANOVA followed by Tukey's multiple comparisons test.

f) Representative images of MTs assembled in lysates at different GFP-CLIP170 (white) concentrations after 10 min. More images are shown in Extended Data Fig. 9a. N = 3 from 2 independent lysate preparations.

g) GFP-CLIP170 droplet sizes at three different GFP-CLIP170 concentrations in lysates. Droplet size was measured for all droplets indicated in Extended Data Fig. 9a. N = 38 - 57

GFP-CLIP170 droplets for each dilution from a representative experiment (f) were used. Data are presented as scatter plots with median with 95% confidence interval (CI). Significance was tested using one-way ANOVA followed by Tukey's multiple comparisons test.

h) Droplet distance determined as in (e) from all GFP density profiles as indicated in Extended Data Fig. 9b. N = 40 - 103 GFP-CLIP170 droplets from a representative experiment (f). Data are presented as scatter plots with median with 95% confidence interval (CI). Significance was tested using one-way ANOVA followed by Tukey's multiple comparisons test.

Numerical data are available in source data.

Figure 8: Generation of MTs from CLIP170-tubulin co-condensates

a) Schematic representation of the work flow. In step 1, MTs are grown from lysates of HeLa Kyoto cells stably expressing mCherry-α-tubulin, and transfected with GFP-CLIP170. In step 2, after CLIP170 droplet formation, fresh lysate from mCherry-α-tubulin-expressing HeLa Kyoto cells was added and MT polymerisation was observed. MTs were then stained with YL1/2 antibody in step 3.

b) Images of MTs polymerised in step 1 show that mCherry-α-tubulin accumulates in GFP-CLIP170 droplets. N = 3 independent TIRF assays from 2 independent cell lysate preparations.

c) Time-lapse images of de-novo MT growth in step 2. Most MTs grow from GFP-CLIP170 droplets formed in step 1 (see Supplementary Video 18c). N = 3 independent TIRF assays from 2 independent cell lysate preparations.

d) At the end of the time-lapse imaging in step 2 (c), MTs were stained with the antibody YL1/2 for better visualisation. Note that MTs have grown almost exclusively from GFP-CLIP170 droplets (merge also shown in Supplementary Video 18d).

Numerical data are available in source data.

REFERENCES

1. Hirokawa, N., Noda, Y., Tanaka, Y. & Niwa, S. Kinesin superfamily motor proteins and intracellular transport. *Nat Rev Mol Cell Biol* **10**, 682-696 (2009).
2. Veigel, C. & Schmidt, C.F. Moving into the cell: single-molecule studies of molecular motors in complex environments. *Nat Rev Mol Cell Biol* **12**, 163-176 (2011).
3. Roberts, A.J., Kon, T., Knight, P.J., Sutoh, K. & Burgess, S.A. Functions and mechanics of dynein motor proteins. *Nat Rev Mol Cell Biol* **14**, 713-726 (2013).
4. McNally, F.J. & Roll-Mecak, A. Microtubule-severing enzymes: From cellular functions to molecular mechanism. *J Cell Biol* **217**, 4057-4069 (2018).
5. Akhmanova, A. & Steinmetz, M.O. Control of microtubule organization and dynamics: two ends in the limelight. *Nat Rev Mol Cell Biol* **16**, 711-726 (2015).
6. Olmsted, J.B. Microtubule-associated proteins. *Annu Rev Cell Biol* **2**, 421-457 (1986).
7. Mandelkow, E. & Mandelkow, E.-M. Microtubules and microtubule-associated proteins. *Curr Opin Cell Biol* **7**, 72-81 (1995).
8. Bodakuntla, S., Jijumon, A.S., Villablanca, C., Gonzalez-Billault, C. & Janke, C. Microtubule-Associated Proteins: Structuring the Cytoskeleton. *Trends Cell Biol* **29**, 804-819 (2019).
9. Dogterom, M. & Surrey, T. Microtubule organization in vitro. *Curr Opin Cell Biol* **25**, 23-29 (2013).
10. Monroy, B.Y. *et al.* A Combinatorial MAP Code Dictates Polarized Microtubule Transport. *Dev Cell* **53**, 60-72 e64 (2020).
11. Hooikaas, P.J. *et al.* MAP7 family proteins regulate kinesin-1 recruitment and activation. *J Cell Biol* **218**, 1298-1318 (2019).
12. Alfaro-Aco, R. & Petry, S. Building the Microtubule Cytoskeleton Piece by Piece. *J Biol Chem* **290**, 17154-17162 (2015).
13. Field, C.M., Pelletier, J.F. & Mitchison, T.J. Xenopus extract approaches to studying microtubule organization and signaling in cytokinesis. *Methods Cell Biol* **137**, 395-435 (2017).
14. Bergman, Z.J., Wong, J., Drubin, D.G. & Barnes, G. Microtubule dynamics regulation reconstituted in budding yeast lysates. *J Cell Sci* **132**, jcs.219386 (2018).
15. Soppina, V. *et al.* Dimerization of mammalian kinesin-3 motors results in superprocessive motion. *Proc Natl Acad Sci U S A* **111**, 5562-5567 (2014).
16. Sun, F., Zhu, C., Dixit, R. & Cavalli, V. Sunday Driver/JIP3 binds kinesin heavy chain directly and enhances its motility. *EMBO J* **30**, 3416-3429 (2011).
17. Cai, D., Verhey, K.J. & Meyhofer, E. Tracking single Kinesin molecules in the cytoplasm of mammalian cells. *Biophys J* **92**, 4137-4144 (2007).
18. Ayloo, S. *et al.* Dynactin functions as both a dynamic tether and brake during dynein-driven motility. *Nat Commun* **5**, 4807 (2014).
19. Schimert, K.I., Budaitis, B.G., Reinemann, D.N., Lang, M.J. & Verhey, K.J. Intracellular cargo transport by single-headed kinesin motors. *Proc Natl Acad Sci U S A* **116**, 6152-6161 (2019).
20. Budaitis, B.G. *et al.* Neck linker docking is critical for Kinesin-1 force generation in cells but at a cost to motor speed and processivity. *Elife* **8**, e44146 (2019).
21. Blasius, T.L. *et al.* Sequences in the stalk domain regulate auto-inhibition and ciliary tip localization of the immotile kinesin-4 KIF7. *J Cell Sci* **134**, jcs258464 (2021).
22. Pierre, P., Pepperkok, R. & Kreis, T.E. Molecular characterization of two functional domains of CLIP-170 in vivo. *J Cell Sci* **107 (Pt 7)**, 1909-1920 (1994).

23. Jeong, J.-Y. *et al.* One-step sequence- and ligation-independent cloning as a rapid and versatile cloning method for functional genomics studies. *Appl Environ Microbiol* **78**, 5440-5443 (2012).
24. Cleveland, D.W. Autoregulated control of tubulin synthesis in animal cells. *Curr Opin Cell Biol* **1**, 10-14 (1989).
25. Lin, Z. *et al.* TTC5 mediates autoregulation of tubulin via mRNA degradation. *Science* **367**, 100-104 (2020).
26. Hiller, G. & Weber, K. Radioimmunoassay for tubulin: a quantitative comparison of the tubulin content of different established tissue culture cells and tissues. *Cell* **14**, 795-804 (1978).
27. Roll-Mecak, A. & Vale, R.D. Structural basis of microtubule severing by the hereditary spastic paraplegia protein spastin. *Nature* **451**, 363-367 (2008).
28. Akhmanova, A. & Steinmetz, M.O. Tracking the ends: a dynamic protein network controls the fate of microtubule tips. *Nat Rev Mol Cell Biol* **9**, 309-322 (2008).
29. Wieczorek, M., Bechstedt, S., Chaaban, S. & Brouhard, G.J. Microtubule-associated proteins control the kinetics of microtubule nucleation. *Nat Cell Biol* **17**, 907-916 (2015).
30. Brandt, R. & Lee, G. Functional organization of microtubule-associated protein tau. Identification of regions which affect microtubule growth, nucleation, and bundle formation in vitro. *J Biol Chem* **268**, 3414-3419 (1993).
31. Spector, I., Shochet, N.R., Kashman, Y. & Groweiss, A. Latrunculins: novel marine toxins that disrupt microfilament organization in cultured cells. *Science* **219**, 493-495 (1983).
32. Coue, M., Brenner, S.L., Spector, I. & Korn, E.D. Inhibition of actin polymerization by latrunculin A. *FEBS Lett* **213**, 316-318 (1987).
33. Eichenmüller, B., Everley, P., Palange, J., Lepley, D. & Suprenant, K.A. The human EMAP-like protein-70 (ELP70) is a microtubule destabilizer that localizes to the mitotic apparatus. *J Biol Chem* **277**, 1301-1309 (2002).
34. Bulinski, J.C. & Bossler, A. Purification and characterization of ensconsin, a novel microtubule stabilizing protein. *J Cell Sci* **107 (Pt 10)**, 2839-2849 (1994).
35. Metzger, T. *et al.* MAP and kinesin-dependent nuclear positioning is required for skeletal muscle function. *Nature* **484**, 120-124 (2012).
36. Yadav, S., Verma, P.J. & Panda, D. C-terminal region of MAP7 domain containing protein 3 (MAP7D3) promotes microtubule polymerization by binding at the C-terminal tail of tubulin. *PLoS One* **9**, e99539 (2014).
37. Sung, H.-H. *et al.* Drosophila ensconsin promotes productive recruitment of Kinesin-1 to microtubules. *Dev Cell* **15**, 866-876 (2008).
38. Nédélec, F.J., Surrey, T., Maggs, A.C. & Leibler, S. Self-organization of microtubules and motors. *Nature* **389**, 305-308 (1997).
39. Backer, C.B., Gutzman, J.H., Pearson, C.G. & Cheeseman, I.M. CSAP localizes to polyglutamylated microtubules and promotes proper cilia function and zebrafish development. *Mol Biol Cell* **23**, 2122-2130 (2012).
40. Bompard, G. *et al.* CSAP Acts as a Regulator of TTLL-Mediated Microtubule Glutamylation. *Cell Rep* **25**, 2866-2877 e2865 (2018).
41. Tokunaga, M., Imamoto, N. & Sakata-Sogawa, K. Highly inclined thin illumination enables clear single-molecule imaging in cells. *Nat Methods* **5**, 159-161 (2008).
42. Cuveillier, C. *et al.* MAP6 is an intraluminal protein that induces neuronal microtubules to coil. *Sci Adv* **6**, eaaz4344 (2020).

43. Leung, C.L., Sun, D., Zheng, M., Knowles, D.R. & Liem, R.K. Microtubule actin cross-linking factor (MACF): a hybrid of dystonin and dystrophin that can interact with the actin and microtubule cytoskeletons. *J Cell Biol* **147**, 1275-1286 (1999).
44. Yang, Y. *et al.* An essential cytoskeletal linker protein connecting actin microfilaments to intermediate filaments. *Cell* **86**, 655-665 (1996).
45. Sun, D., Leung, C.L. & Liem, R.K. Characterization of the microtubule binding domain of microtubule actin crosslinking factor (MACF): identification of a novel group of microtubule associated proteins. *J Cell Sci* **114**, 161-172 (2001).
46. Matus, A. Microtubule-associated proteins: their potential role in determining neuronal morphology. *Annu Rev Neurosci* **11**, 29-44 (1988).
47. Kindler, S., Schulz, B., Goedert, M. & Garner, C.C. Molecular structure of microtubule-associated protein 2b and 2c from rat brain. *J Biol Chem* **265**, 19679-19684 (1990).
48. Ludin, B., Ashbridge, K., Funfschilling, U. & Matus, A. Functional analysis of the MAP2 repeat domain. *J Cell Sci* **109 (Pt 1)**, 91-99 (1996).
49. Murphy, D.B. & Borisy, G.G. Association of high-molecular-weight proteins with microtubules and their role in microtubule assembly in vitro. *Proc Natl Acad Sci U S A* **72**, 2696-2700 (1975).
50. Bowne-Anderson, H., Hibbel, A. & Howard, J. Regulation of Microtubule Growth and Catastrophe: Unifying Theory and Experiment. *Trends Cell Biol* **25**, 769-779 (2015).
51. Roger, B., Al-Bassam, J., Dehmelt, L., Milligan, R.A. & Halpain, S. MAP2c, but not tau, binds and bundles F-actin via its microtubule binding domain. *Curr Biol* **14**, 363-371 (2004).
52. Sandoval, I.V. & Vandekerckhove, J.S. A comparative study of the in vitro polymerization of tubulin in the presence of the microtubule-associated proteins MAP2 and tau. *J Biol Chem* **256**, 8795-8800 (1981).
53. Monroy, B.Y. *et al.* Competition between microtubule-associated proteins directs motor transport. *Nat Commun* **9**, 1487 (2018).
54. Siahaan, V. *et al.* Kinetically distinct phases of tau on microtubules regulate kinesin motors and severing enzymes. *Nat Cell Biol* **21**, 1086-1092 (2019).
55. Kielar, M. *et al.* Mutations in Eml1 lead to ectopic progenitors and neuronal heterotopia in mouse and human. *Nat Neurosci* **17**, 923-933 (2014).
56. Uzquiano, A. *et al.* Mutations in the Heterotopia Gene Eml1/EML1 Severely Disrupt the Formation of Primary Cilia. *Cell Rep* **28**, 1596-1611 e1510 (2019).
57. Kellogg, E.H. *et al.* Near-atomic model of microtubule-tau interactions. *Science* **360**, 1242-1246 (2018).
58. Adib, R. *et al.* Mitotic phosphorylation by NEK6 and NEK7 reduces the microtubule affinity of EML4 to promote chromosome congression. *Sci Signal* **12**, 10.1126/scisignal.aaw2939 (2019).
59. Manka, S.W. & Moores, C.A. Microtubule structure by cryo-EM: snapshots of dynamic instability. *Essays Biochem* **62**, 737-751 (2018).
60. Zhang, R., Roostalu, J., Surrey, T. & Nogales, E. Structural insight into TPX2-stimulated microtubule assembly. *Elife* **6**, e30959 (2017).
61. Su, C.-C. *et al.* A 'Build and Retrieve' methodology to simultaneously solve cryo-EM structures of membrane proteins. *Nat Methods* **18**, 69-75 (2021).
62. Perez, F., Diamantopoulos, G.S., Stalder, R. & Kreis, T.E. CLIP-170 highlights growing microtubule ends in vivo. *Cell* **96**, 517-527 (1999).
63. Bieling, P. *et al.* Reconstitution of a microtubule plus-end tracking system in vitro. *Nature* **450**, 1100-1105 (2007).

64. Bieling, P. *et al.* CLIP-170 tracks growing microtubule ends by dynamically recognizing composite EB1/tubulin-binding sites. *J Cell Biol* **183**, 1223-1233 (2008).
65. Pierre, P., Scheel, J., Rickard, J.E. & Kreis, T.E. CLIP-170 links endocytic vesicles to microtubules. *Cell* **70**, 887-900 (1992).
66. Wu, Y.-F.O. *et al.* Overexpression of the microtubule-binding protein CLIP-170 induces a +TIP network superstructure consistent with a biomolecular condensate. *bioRxiv*, 2021.2001.2001.424687 (2021).
67. Alberti, S., Gladfelter, A. & Mittag, T. Considerations and Challenges in Studying Liquid-Liquid Phase Separation and Biomolecular Condensates. *Cell* **176**, 419-434 (2019).
68. Tan, R. *et al.* Microtubules gate tau condensation to spatially regulate microtubule functions. *Nat Cell Biol* **21**, 1078-1085 (2019).
69. King, M.R. & Petry, S. Phase separation of TPX2 enhances and spatially coordinates microtubule nucleation. *Nat Commun* **11**, 270 (2020).
70. Steigemann, P. *et al.* Aurora B-mediated abscission checkpoint protects against tetraploidization. *Cell* **136**, 473-484 (2009).
71. Roux, K.J., Kim, D.I., Burke, B. & May, D.G. BioID: A Screen for Protein-Protein Interactions. *Curr Protoc Protein Sci* **91**, 19 23 11-19 23 15 (2018).
72. Ben-Sasson, A.J. *et al.* Design of biologically active binary protein 2D materials. *Nature* **589**, 468-473 (2021).
73. Dogterom, M. & Koenderink, G.H. Actin-microtubule crosstalk in cell biology. *Nat Rev Mol Cell Biol* **20**, 38-54 (2019).
74. Gentili, M. *et al.* Transmission of innate immune signaling by packaging of cGAMP in viral particles. *Science* **349**, 1232-1236 (2015).

METHODS

Mouse lines

All the C57BL/6N animals in this study were used in accordance with the recommendations of the European Community (2010/63/UE). Experimental procedures were specifically approved by the ethics committee of the Institut Curie CEEA-IC #118 (authorisation n°*04395.03* given by National Authority) in compliance with the international guidelines.

Cloning using Sequence and Ligation Independent Cloning (SLIC)

To determine the most complete, annotated open reading frames (ORFs) for proteins of interest, we searched public databases such as NCBI or EMBL-EBI, and compared murine and human ORF variants. The longest identified ORF was chosen for cloning. The amino- and carboxy- terminal boundaries of the MAPs were determined as follows: We first identified the longest annotated open reading frames (ORFs) for the proteins of interest from public databases such as NCBI or EMBL-EBI. As the expression profiles for many MAPs were not well known, we amplified the ORF of interest from a panel of cDNAs from brain, testes and cell lines. Using this approach, we succeeded amplifying most ORFs of interest, and strikingly in some cases our approach allowed us to identify splice isoforms (Supplementary Table 1), as well as previously undescribed ORFs such as for DCX (Supplementary Table 1; DCX_L). Because of the particularly large size of the MT-actin crosslinking factors MACF1and MACF2 (5328 and 7718 amino acids respectively), we cloned ~1000 amino acids upstream from the carboxy-terminal region, which contain the MT-binding domains[43].

Primers were designed from the start codon until the stop codon, omitting the stop codon for C-terminal tagging. All PCR primers are listed in Supplementary Table 1. Primers contain standardised homology regions for the insertion into the target vector as shown in Extended Data Fig. 1a. ORFs were PCR-amplified with Q5 High-Fidelity 2× Master Mix (NEB) from cDNA libraries retro-transcribed with First Strand cDNA synthesis kit (Cytiva) from RNA purified from mouse tissue (here we mostly used brain and testis cDNA). As a target vector, we used a pTRIP vector[74] variant with a CMV-enhanced chicken beta-actin (CAG) promoter[75] that allows expansion of our pipeline to primary cells, such as neurons. The vector is linearized with NheI for C-terminal tagging, or BsrGI/BamHI for N-terminal tagging (Extended Data Fig. 1a). PCR product and linearized vector were gel-purified with QIAquick

gel extraction kit (Qiagen), and fused using the SLIC method[23] (Extended Data Fig. 1b): 2 µl linearized vector was mixed with 7 µl PCR product, 1 µl buffer and 0.3 µl T4 DNA polymerase (NEB) on ice. After 2.5 min incubation at room temperature, it was re-transferred on ice, 100 µl competent E. coli cells were added and incubated for 30 min on ice, heat-shocked for 45 s at 42°C, and re-incubated for 10 min on ice. Bacteria were recovered in LB medium at 37°C, 1 h before spreading onto ampicillin-containing LB-agar. Single colonies were amplified for plasmid DNA purification, and plasmids were digested with restriction enzymes initially used to linearize the plasmid to verify presence of the inserted ORFs. Positive clones were sequenced. In case different sizes of ORFs are detected after cloning, we analysed all variants to identify potential splice isoforms of the protein of interest.

Immunostaining and imaging

4×10^4 U-2 OS cells (ATCC HTB-96), seeded on coverslips in 24-well dishes in DMEM complete medium (supplemented with 10% (v/v) FBS, 2 mM L-Glutamine, and 1× Penicillin-Streptomycin (Pen Strep; Life Technologies)) were transfected with expression vectors (Supplementary Table 1). Cells were fixed 24 or 48 h after transfection with a protocol preserving the cytoskeleton[76]: Cells were incubated 10 min with Hank's Balanced Salt solution (HBSS), 10 min in MT-stabilising buffer (MTSB) containing the crosslinker DSP (dithiobis(succinimidyl propionate); Thermo Fisher Scientific), followed by 4% paraformaldehyde in MTSB (Electron Microscopy Sciences,) for 15 min. Cells were permeabilised with 0.5% Triton X-100 (Sigma-Aldrich) in MTSB for 5 min, followed by blocking in 5% bovine serum albumin (BSA; Sigma-Aldrich) in PBS containing 0.1% Triton X-100 (PBS-T). Primary (anti-α-tubulin antibody 12G10, 1:1,000) and secondary antibodies (goat anti-mouse Alexa Fluor 568, 1:1,000; Thermo Fisher Scientific), both diluted in PBS-T containing 5% BSA, were incubated for 1 h each. Coverslips were mounted using ProLong Gold anti-fade medium (Thermo Fisher Scientific). Images were acquired using a Leica Optigrid microscope equipped with a 63× (numerical aperture 1.40) oil immersion objective and the ORCA-Flash4.0 camera (Hamamatsu) set at binning 1×1. The microscope was operated through Leica MM AF imaging software. Images were processed using Fiji[77] and Adobe Photoshop. Final figures were prepared using Adobe Illustrator.

Live-cell imaging

875 2×10^4 U-2 OS (ATCC HTB-96) cells/well were seeded into 4-well glass-bottomed dishes
876 (Ibidi) and transfected with GFP-CLIP170 (1 µg of plasmid DNA per well) using jetPEI
877 transfection reagent according to manufacturer's protocol. 8 h after transfection, cells were
878 imaged at Nikon Ti-E spinning disk inverted confocal laser microscope equipped with a 60×
879 oil TIRF NA 1.49 objective and an ORCA-Flash 4.0 camera (Hamamatsu) operated through
880 MetaMorph® software. Time-lapse images of GFP fluorescence and bright-field images were
881 taken every 5 min for 10 h. The focus plane was maintained by Nikon perfect focus system.
882 During the imaging, the microscope was at 37°C and 5% CO_2. The image stacks were
883 processed with Fiji, and videos were mounted with Adobe After Effects.

884

885 **Preparation of cell lysates**

886 2×10^6 HEK 293 cells (Human embryonic kidney cells; ATCC CRL-1573) were seeded on six
887 22-cm^2 dishes per plasmid. Cells at ~80% confluency in DMEM complete medium were
888 transfected using jetPEI (5 µg of DNA and 10 µl of jetPEI in serum-free DMEM with 2 mM
889 L-Glutamine and 1× PenStrep per dish) following the manufacturer's guidelines. After 24 h,
890 GFP expression levels were checked by fluorescence microscopy. At high expression levels
891 (strong GFP fluorescence) cells were harvested, while cells with low-expressing MAPs were
892 harvested after 48 h. The same protocol was followed for generating lysates from HeLa Kyoto
893 cells expressing mCherry-α-tubulin.

894 After media removal, cells were gently washed with 1.5 ml warm PBS per dish, detached with
895 500 µl of trypsin-EDTA per dish, immediately collected in 2 ml of warm DMEM complete
896 media, and transferred to a falcon tube for centrifugation (453×g, 4°C, 10 min; Fig. 1a). the
897 supernatant was removed, and the cell pellet was resuspended in 150-300 µl cold BRB80
898 buffer (80 mM K-Pipes pH 6.8, 1 mM EGTA and 1 mM $MgCl_2$) containing 0.05% Triton-
899 X100 and protease inhibitors (10 µg/ml leupeptin, aprotinin and 4-(2-aminoethyl)-
900 benzenesulfonyl fluoride; Sigma-Aldrich). After transfer to 1.5-ml Beckman ultracentrifuge
901 tubes, cells were lysed by pipetting up down on ice for another 5-8 min and sonicated with
902 three short pulses using the 6.5-mm probe (Branson), setting "Output control" 1, "Duty cycle"
903 10%. Samples were ultra-centrifuged in the Beckman TLA 55 rotor at 33,800×g, 4°C for
904 25 min in the Beckman Coulter Optima MAX-XP ultracentrifuge. Supernatants were
905 aliquoted to 5-10 µl, snap-frozen in liquid nitrogen, and stored at -80°C for up to 1 month. All
906 steps after cell collection are strictly performed on ice.

Protein quantification and immunoblot

We controlled overall protein concentrations in lysates to assure consistent tubulin levels in our assays (~3% of the total protein in cultured cells is tubulin[26]) using Bicinchoninic acid protein assay[78] (BCA; Thermo Fisher Scientific) following the manufacturer instructions. BCA reagent was freshly prepared for each experiment. A sample-to-reagent ratio of 1:8 was incubated at 37°C for 30 min, and absorbance was measured at 562 nm with TriStar² LB 942 Multimode Microplate Reader with MikroWin 2010 software (Berthold). Absorbance values of a BSA standard dilution series were plotted and fitted to a linear equation and obtained the total protein concentration of our samples[79].

The concentration of GFP-MAPs in the lysates was quantified for one specific experiment (Fig. 4) using immunoblot. A dilution series of purified GFP protein of known concentration as standard was run together with a dilution series of lysates expressing MACF1_C1023-GFP (Fig. 4a). The samples were boiled for 5 min with 2× Laemmli sample buffer (4% SDS (VWR), 160 mM Tris-HCl, pH 6.8, 180 mM DTT (Sigma-Aldrich), 20% (w/v) glycerol (VWR) and bromophenol blue), ran on a 10% SDS-PAGE gel, and transferred onto a nitrocellulose membrane with Trans-Blot Turbo system (Bio-Rad) using transfer packs (Bio-Rad). Membranes were blocked for 1 h with 5% non-fat milk in 50 mM Tris-buffered saline (TBS; 50 mM Tris-HCl, pH 7.6, 150 mM NaCl) with 0.1% Tween 20 (Sigma-Aldrich) (TBS-T), followed by 1.5 h incubation in rabbit anti-GFP antibody (1:2,500; Torrey Pines Biolabs TP-401, in 5% non-fat milk in TBS-T). After three washes with TBS-T, the membrane was incubated with secondary HRP-coupled goat anti–rabbit antibody (1:10,000; Thermo Fisher Scientific) for 45 min, followed by three TBS-T washes. The membrane was incubated for 1 min in Clarity Western ECL Substrate (Bio-Rad) and then imaged using the Fusion FX imaging system (Vilber). Values of the known concentration of purified GFP were used to obtain a standard curve[80], from which concentrations of MACF1_C1023-GFP were deduced (Fig. 4a).

Cleaning of glass slides and assembly of flow chambers

TIRF flow chambers were prepared following a modified protocol from reference[81]. Glass slides (76×26 mm; Thermo Fisher Scientific) and coverslips (22×22 mm; thickness no. 1.5, VWR 631-0125) were wiped with Kimtech paper, and added one by one into separate clean

bottles with 100% acetone, which were sonicated in a water bath (Diagenode Bioruptor) for 15 min at room temperature. Acetone was discarded, and slides and coverslips were rinsed with ultra-pure water. The water was exchanged and bottles were sonicated as before, after which the water was exchanged for 100% ethanol, and sonicated as before. Finally, ethanol was exchanged for fresh 100% ethanol, in which the slides and coverslips could be stored for up to one month.

TIRF flow chambers were assembled by following protocols from references[81, 82]. Glass slides were removed from ethanol, flamed and placed on a clean surface. Four long strips of double-sided adhesive tape were pasted to obtain three chambers on a single glass slide. The double-sided tape was pressed to the slides with the backside of forceps to fix it firmly, and the protective sheet was peeled off with forceps. A fresh coverslip stored in ethanol was flamed, placed on top of sticky tape strips, and pressed gently with the rear side of the forceps. The typical volume of a single TIRF chamber is around 7-10 µl. Prepared chambers can be stored at room temperature for a few weeks in a dust-free space.

Preparation of GMPCPP seeds

Single-cycled GMPCPP-MT seeds were prepared in 60 µl of 20 µM unlabelled pig brain tubulin (purified as in ref.[83]) and 10-15% rhodamine-labelled brain tubulin, or Fluorescent HiLyte 647 porcine brain tubulin (Cytoskeleton Inc.) in BRB80 buffer. After centrifugation (98,400×g, 4°C, 30 min) to remove insoluble components, the supernatant containing soluble tubulin was transferred to a fresh tube, adjusted to 0.5 mM GMPCPP (Jena Biosciences), first incubated on ice for 5 min, followed by 37°C for 1 h. The polymerised GMPCPP MTs were pelleted at 37°C, 20,000 g for 10 min, and subsequently washed with warm BRB80 buffer (20,000 g, 3 min, 37°C). Finally, the GMPCPP-MT pellet was resuspended in warm BRB80 buffer (75 µl) containing 10% (v/v) glycerol, snap-frozen in 2-5 µl aliquots, and stored at -80°C. For longer storage at -80°C, double-cycled GMPCPP seeds were prepared as described in ref.[81]. For this, the GMPCPP-MT pellet obtained after warm centrifugation (20,000×g, 3 min, 37°C) was resuspended in cold BRB80 buffer, followed by frequent pipetting on ice for 20 min to efficiently depolymerise MTs. For the second round of MT polymerisation, tubulin was incubated for 5 min with 0.5 mM of GMPCPP on ice, and then for 30 min at 37°C. The pelleting, washing, resuspension and storage steps are same as for single-cycled MT seeds.

For the cryo-electron microscopy, GMPCPP-MT seeds were prepared without labelled tubulin. 50 μM purified goat brain tubulin (purified as in ref.[84]) in BRB80 buffer was polymerised with 1 mM GMPCPP at 37°C for 2 h, spun on warm 50% BRB80 sucrose cushion in a table-top high-speed centrifuge, and resuspended in two volumes of warm BRB80 buffer.

Protein purification

To attach MTs in the imaging chambers, we used a truncated version (the first 555 amino acids) of the mouse kinesin-1 KIF5B carrying the walker mutation Thr92Asn[85]. The protein was expressed in E. coli as 6His-mKIF5B_N555^{Thr92Asn86} and was isolated by batch purification as described before[87]. Bacteria were grown at 37°C to an optical density at 600 nm (OD^{600}) of 0.6-0.8, and protein expression was induced with 0.5 mM IPTG (isopropyl-1-thio-β-D-galactopyranoside) at 20°C for 12 h. Cells were harvested at 4,500×g for 15 min, and lysed in 50 mM Tris-HCl pH 8.0, 100 mM NaCl, 30 mM imidazole pH 8.0, 10% (w/v) glycerol, 0.05% Triton-X100, and 1× protease inhibitor cocktail by sonication. The lysate was cleared by centrifugation at 80,000×g for 12 min at 4°C, and gently rotated for 2 h (4°C) with chelating sepharose (GE Healthcare) resin functionalised with $NiSO_4$ (250 μl resin for 1 l initial E. coli culture). The resin was sedimented at 500×g for 2 min, and washed 3× with 2 ml of wash buffer (50 mM Tris-HCl pH 8.0, 100 mM NaCl, 30 mM imidazole pH 8.0, 10% (w/v) glycerol) by gently mixing the resin in the buffer (with a cut pipette tip) followed by a sedimentation step (500×g, 2 min). The protein was eluted with 50 mM Tris-HCl pH 8.0, 20 mM NaCl, 250 mM imidazole pH 8.0 and 5% (w/v) glycerol.

Purification of GFP from HEK 293 cells via Strep-Tag®II-Strep-Tactin affinity purification was adapted from a previous protocol[11], with minor modifications. Twin-Strep-Tag®II (IBA GmbH, Göttingen) was cloned into pTRIP vector as C-terminal fusion to GFP. HEK 293 cells in five 14.5-cm cell culture dishes at ~50% confluency were transfected, and harvested after 24 h by subsequent washing with PBS, detachment with 0.05% Trypsin-EDTA and collection in PBS. To remove traces of Trypsin-EDTA, cells were washed one more time with PBS and cold centrifugation. Cells were resuspended in 800 μl cold lysis buffer (50 mM HEPES pH 7.4, 300 mM NaCl, 1 mM $MgCl_2$, 0.5% Triton-X-100, 1 mM DTT, 100 mM EGTA, 1× protease inhibitors cocktail) and incubated on ice for 15 min with occasional pipetting to break cells. The lysate was centrifuged at 18,500×g for 15 min at 4°C. The supernatant was

added to 250 µl pre-equilibrated and blocked Streptactin Sepharose® High Performance beads (Cytiva) and incubated for 45 min at 4°C by slow rotation. The beads were washed 3× in high-salt wash buffer (50 mM HEPES pH 7.4, 300 mM NaCl, 1 mM $MgCl_2$, 0.5% Triton-X100, 1 mM DTT), 3× in pre-elution-wash buffer (50 mM HEPES pH 7.4, 150 mM NaCl, 1 mM $MgCl_2$, 0.05% Triton-X100, 1 mM DTT, 1 mM EGTA), and eluted with 100-250 µl elution buffer (50 mM HEPES pH 7.4, 150 mM NaCl, 1 mM $MgCl_2$, 0.05% Triton-X100, 1 mM DTT, 1 mM EGTA, 2.5 mM d-desthiobiotin; Sigma-Aldrich).

Eluted proteins were aliquoted, snap-frozen in liquid nitrogen and stored at -80°C. The protein purity was examined via SDS-PAGE and Coomassie Brilliant Blue staining.

MT reconstitution and TIRF microscopy

Flow chambers were first blocked for 5 min with 50 µg/ml of β-Casein (Sigma-Aldrich) in BRB80, and subsequently incubated with 0.75 µM of 6His-mKIF5B_N555^{Thr92Asn} for 5 min. GMPCPP seeds resuspended in warm BRB80 were flushed into the chamber and incubated for 5 min for immobilisation. Excess unattached seeds were washed out using warm BRB80 buffer, after which the density of the seeds in the chamber was verified under the TIRF microscope.

A fresh tube of cell lysate stored at -80°C was thawed, adjusted (if required) to 8 µg/µl total protein concentration in BRB80 buffer, flushed into the prepared imaging chamber and immediately transferred to a Nikon TiE azimuthal TIRF using an iLas-2 system (Gataca Systems) on an inverted microscope with a 100× TIRF NA 1.49 oil objective equipped with Nikon perfect focus system. The imaging area was 68.1×68.1 µm and images were captured by an Evolve EM-CCD camera using MetaMorph® software with a Modular interface for TIRF. Flow chambers were illuminated at 488 nm (Stradus® Vortran, 150 mW) for GFP-tagged proteins, and at 561 nm (Jive™ Cobolt, 100 mW) for GMPCPP seeds (rhodamine-labelled brain tubulin; Cytoskeleton Inc.), or mCherry-tagged proteins for a total duration of 11.612 min with a frame interval of 1.98 s. These settings were strictly followed in all TIRF microscopy assays shown here.

After completion of time-lapse imaging, MTs and actin were visualised. Chambers were washed with warm BRB80 buffer, followed by a 5-min incubation with YL1/2 antibody (1:100 in BRB80). Chambers were washed again, and Alexa 565-labelled anti-rat antibody (1:100 in BRB80; Thermo Fisher Scientific) was flushed in for 5 min. After another wash,

500 nM SiR-Actin (Spirochrome) was flushed in for 5 min incubation, and subsequently washed out with BRB80. Still images of GFP-tagged protein (at 488 nm), YL1/2-labelled MTs (at 561 nm) and the SiR-Actin-stained actin filaments (at 642 nm; Stradus^{TM} Vortran, 165 mW) were acquired with the TIRF microscope. All above-described steps were repeated in the presence of 11 µM Latrunculin A (Sigma-Aldrich), to prevent actin polymerisation[32].

For the experiments with 1,6-Hexanediol (Sigma-Aldrich), GFP-CLIP170 cell lysates were initially incubated in the microscopy chamber containing GMPCPP MT seeds, and the formation of droplet-like assemblies was imaged for 3 min at 1 fps. Subsequently, BRB80 with 0% (control), 5% and 10% (w/v) 1,6-Hexanediol was flushed into the chambers, and the acquisition was continued for another 3 min at 1 fps.

Image and data analysis for TIRF assays

TIRF images were processed using Fiji software[77]. Some raw images and videos underwent shading correction with a homemade macro (https://doi.org/10.5281/zenodo.5648066) by Gaussian smoothing with a standard deviation of 30 sigma to approximate a shading image. Flat-field corrected images were obtained by subtracting Gaussian-smoothed from raw images. Videos are 20× accelerated for mounting with Adobe After Effects. Still images were treated and quantitatively analysed with Fiji software, adjusted and mounted with Adobe Photoshop and Illustrator.

The width of CSAP-induced MT coils (Fig. 3c; Extended Data Fig. 7a) and diameter of MACF1_C1023-induced MT hooks (Fig. 3d; Extended Data Fig. 7b) were determined by manually drawing lines over these structures, and extracting their length in Fiji.

CLIP170 droplet diameters was determined by drawing lines across droplets perpendicular to the MT, along which fluorescence-intensity distribution was measured, and Gaussian fitting was used to extract full width at half maxima (FWHM; Fig. 7d,g). This was repeated for all droplets individually. For CLIP170 droplet spacing (Fig. 7e,h), we obtained GFP-CLIP170 intensity profiles from line scans along individual MTs (Fig. 7c; Extended Data Fig. 9). Droplet spacing was determined by automatically detecting local maxima with the Fiji BAR plugin (https://imagej.net/BAR), with a variable value as minimum peak amplitude that covers all local maxima. Coordinates of maxima in 1D were transferred to Microsoft Excel for sorting and calculating distances. All data were finally transferred to GraphPad Prism software for plotting and statistical analyses.

Electron microscopy

Quantifoil gold holey carbon grids R 1.2/1.3 were glow-discharged in a GloQube Glow Discharge (Quorum Technologies) system for 90 s. Sample application and vitrification were carried out in a Vitrobot Mark IV (ThermoFisher Scientific) set to 25°C and 100% humidity using a Whatman No. 1 filter paper for blotting.

Cell lysates with overexpressed MAPs stored at -80°C were thawed and warmed only before application on the grids. In case of MACF1_C1023-GFP, purified HeLa tubulin[88] was added to accelerate MT formation.

1 µl GMPCPP-MT seeds in warm BRB80 was applied to the grid mounted in the Vitrobot. After 10-20 s for seed adsorption, 3 µl of pre-warmed lysate was applied to the grid, which were blotted after 20-120 s with blot force zero and blot time 3 s before plunging into liquid ethane.

Frozen grids were transferred to an Autoloader under liquid nitrogen and mounted into a Titan Krios (FEI) G3 transmission electron microscope operating at 300 kV and attached to the Falcon III detector. Data were collected with an automated pipeline of EPU software. 30 frames were collected per movie in the linear mode at a dose rate of 1.87 electrons/pixel/s and a total dose of 44.17 electrons/Å^2. Images were collected at a magnification of 59,000×, resulting in 1.38 Å pixel size and a defocus range between -1.8 to -3.0 µm.

Image processing and 3D reconstruction

Images were manually inspected for ice contaminants and filament quality, and unwanted micrographs discarded. EML4 and MACF1_C1024 datasets were not used for further analyses; micrographs in Fig. 6b are representative images. Movie frames of EML1 datasets were motion-corrected using the inbuilt feature of MotionCor2[89] in RELION 3.0[90, 91]. Contrast transfer function (CTF) estimation was done by GCTF[92] on dose-weighted and motion-corrected summed images. Particles were manually boxed using the helical picking option of RELION 3.0[93] (box size 600 Å, overlapping inter-box distance 82 Å). Processing was carried out with RELION 3.0 and customised scripts to reconstruct MTs with a seam (pseudo-helical symmetry)[94]. 2× binned particles were used during the initial stages of processing. Particles were segregated into classes based on protofilament numbers by one

round of 3D classification using low-passed synthetic references of MTs made of different protofilament numbers (11, 12, 13, 14, 15 and 16). The dominant class contained 14-protofilament MTs was further processed. A few cycles of refinement were used to improve the alignment of all the particles. A 14-protofilament MT with pixels doubled for loop regions of S9-S10 and H1-S2 (different in α- and β-tubulin), and low-pass filtered to 6 Å, was used as the reference in these stages[58]. The phi angle was determined for the particles, and the modal value was assigned to all particles in a single MT. This was further checked by 3D classification using low-pass-filtered references of 14-protofilament MTs with enhanced pixels for S9-S10 and H1-S2 loop regions rotated and shifted (by one monomer repeat of 4 nm) to accommodate all possible 28 positions for a 14-protofilament MT with a seam. The segments were flipped to the modal positions and corresponding phi angles were assigned to all segments in a given MT. Finally, refinement was carried out on unbinned aligned particles using a low-pass filtered 14-protofilament MT reference with and without applying helical symmetry. An atomic poly-alanine model of the HeLa cell tubulin dimer (PDB ID:6i2i) was fitted into the symmetrised map in UCSF Chimera[95] and refined manually by model building in Coot[96] followed by real-space refinement in PHENIX[97, 98]. The refined model is available upon request. An atomic model for EML1-GFP could not be generated due to the low-resolution density corresponding to the EML1 region bound to the microtubule lattice. All images and structural superposition with the reconstruction of EML4_N207-bound MT (EMDB 1331; PDB ID 6i2i) were generated in UCSF Chimera[95]. For data collection and processing details, see Supplementary Table 2.

Material availability

Plasmids generated in this study are available upon request.

Data availability

All commercial resources used here are detailed in Supplementary Table 3; primers for molecular cloning are listed in Supplementary Table 1; antibodies are listed in Supplementary Table 4. Source data are provided with this study. All data supporting the findings of this study are available from the corresponding author upon reasonable request.

Code availability

The cryo-EM map for EML1-GFP bound to a MT is deposited in the Electron Microscopy Data Bank (EMDB) under the accession code EMD-32033. Gene sequences of newly identified MAPs (DCX_L, MAP11; see Supplementary Table 1) are deposited at GenBank under the accession codes OK539808 (DCX_L) and OK539809 (MAP11). Deposited data are listed in Supplementary Table 5.

We used mostly free software for the analyses, details of the paid software are included in Supplementary Table 3. Home-made macros used in the analyses (Fig. 7d,g) have been deposited at Zenodo (https://doi.org/10.5281/zenodo.5648066).

Statistics and reproducibility

Experiments in this work were not randomised and no blinding was used during the data analyses, as the experiments were designed and carried out by same group of people. Data were tabulated in Microsoft Excel and statistical analyses were performed using GraphPad Prism software. Whenever statistics is performed, data was pooled from at least three independent experiments. For the comparison of three or more groups, one-way ANOVA was used. P values ≤ 0.05 were considered significant. No statistical method was used to predetermine sample size, and no data were excluded from the analyses.

The exact number of cells, independent TIRF, or cryo-EM experiments, as well as the number of cell lysate preparation used for each experiment are indicated in respective figure legends, and all numerical values used for the quantification are detailed in the source data file (Fig. 1b,c; Fig. 2-4; Fig. 5b; Fig. 7a,b,c,f; Fig. 8b,c; Extended Data Fig. 2-10; Supplementary information Fig. 1, 2).

Method references

75. Alexopoulou, A.N., Couchman, J.R. & Whiteford, J.R. The CMV early enhancer/chicken beta actin (CAG) promoter can be used to drive transgene expression during the differentiation of murine embryonic stem cells into vascular progenitors. *BMC Cell Biol* **9**, 2 (2008).
76. Magiera, M.M. & Janke, C. Investigating tubulin posttranslational modifications with specific antibodies, in *Methods Cell Biol*, Vol. 115, Edn. 2013/08/27. (eds. J.J. Correia & L. Wilson) 247-267 (Academic Press, Burlington; 2013).
77. Schneider, C.A., Rasband, W.S. & Eliceiri, K.W. NIH Image to ImageJ: 25 years of image analysis. *Nat Methods* **9**, 671-675 (2012).
78. Smith, P.K. *et al.* Measurement of protein using bicinchoninic acid. *Anal Biochem* **150**, 76-85 (1985).

79. Brady, P.N. & Macnaughtan, M.A. Evaluation of colorimetric assays for analyzing reductively methylated proteins: Biases and mechanistic insights. *Anal Biochem* **491**, 43-51 (2015).
80. Bodakuntla, S., Jijumon, A.S., Janke, C. & Magiera, M.M. Purification of Tubulin with Controlled Posttranslational Modifications and Isotypes from Limited Sources by Polymerization-Depolymerization Cycles. *J Vis Exp*, 10.3791/61826 (2020).
81. Gell, C. *et al.* Microtubule dynamics reconstituted in vitro and imaged by single-molecule fluorescence microscopy. *Methods Cell Biol* **95**, 221-245 (2010).
82. Li, W. *et al.* Reconstitution of dynamic microtubules with Drosophila XMAP215, EB1, and Sentin. *J Cell Biol* **199**, 849-862 (2012).
83. Castoldi, M. & Popov, A.V. Purification of brain tubulin through two cycles of polymerization-depolymerization in a high-molarity buffer. *Protein Expr Purif* **32**, 83-88 (2003).
84. Vallee, R.B. Reversible assembly purification of microtubules without assembly-promoting agents and further purification of tubulin, microtubule-associated proteins, and MAP fragments. *Methods Enzymol* **134**, 89-104 (1986).
85. Nakata, T. & Hirokawa, N. Point mutation of adenosine triphosphate-binding motif generated rigor kinesin that selectively blocks anterograde lysosome membrane transport. *J Cell Biol* **131**, 1039-1053 (1995).
86. Lacroix, B. *et al.* Tubulin polyglutamylation stimulates spastin-mediated microtubule severing. *J Cell Biol* **189**, 945-954 (2010).
87. Dutta, P. *et al.* Presence of actin binding motif in VgrG-1 toxin of Vibrio cholerae reveals the molecular mechanism of actin cross-linking. *Int J Biol Macromol* **133**, 775-785 (2019).
88. Souphron, J. *et al.* Purification of tubulin with controlled post-translational modifications by polymerization–depolymerization cycles. *Nat Protoc* **14**, 1634–1660 (2019).
89. Zheng, S.Q. *et al.* MotionCor2: anisotropic correction of beam-induced motion for improved cryo-electron microscopy. *Nat Methods* **14**, 331-332 (2017).
90. Scheres, S.H.W. A Bayesian view on cryo-EM structure determination. *J Mol Biol* **415**, 406-418 (2012).
91. Scheres, S.H.W. RELION: implementation of a Bayesian approach to cryo-EM structure determination. *J Struct Biol* **180**, 519-530 (2012).
92. Zhang, K. Gctf: Real-time CTF determination and correction. *J Struct Biol* **193**, 1-12 (2016).
93. He, S. & Scheres, S.H.W. Helical reconstruction in RELION. *J Struct Biol* **198**, 163-176 (2017).
94. Cook, A.D., Manka, S.W., Wang, S., Moores, C.A. & Atherton, J. A microtubule RELION-based pipeline for cryo-EM image processing. *J Struct Biol* **209**, 107402 (2020).
95. Pettersen, E.F. *et al.* UCSF Chimera - a visualization system for exploratory research and analysis. *J Comput Chem* **25**, 1605-1612 (2004).
96. Emsley, P., Lohkamp, B., Scott, W.G. & Cowtan, K. Features and development of Coot. *Acta Crystallogr D Biol Crystallogr* **66**, 486-501 (2010).
97. Adams, P.D. *et al.* PHENIX: a comprehensive Python-based system for macromolecular structure solution. *Acta Crystallogr D Biol Crystallogr* **66**, 213-221 (2010).
98. Afonine, P.V. *et al.* Real-space refinement in PHENIX for cryo-EM and crystallography. *Acta Crystallogr D Struct Biol* **74**, 531-544 (2018).

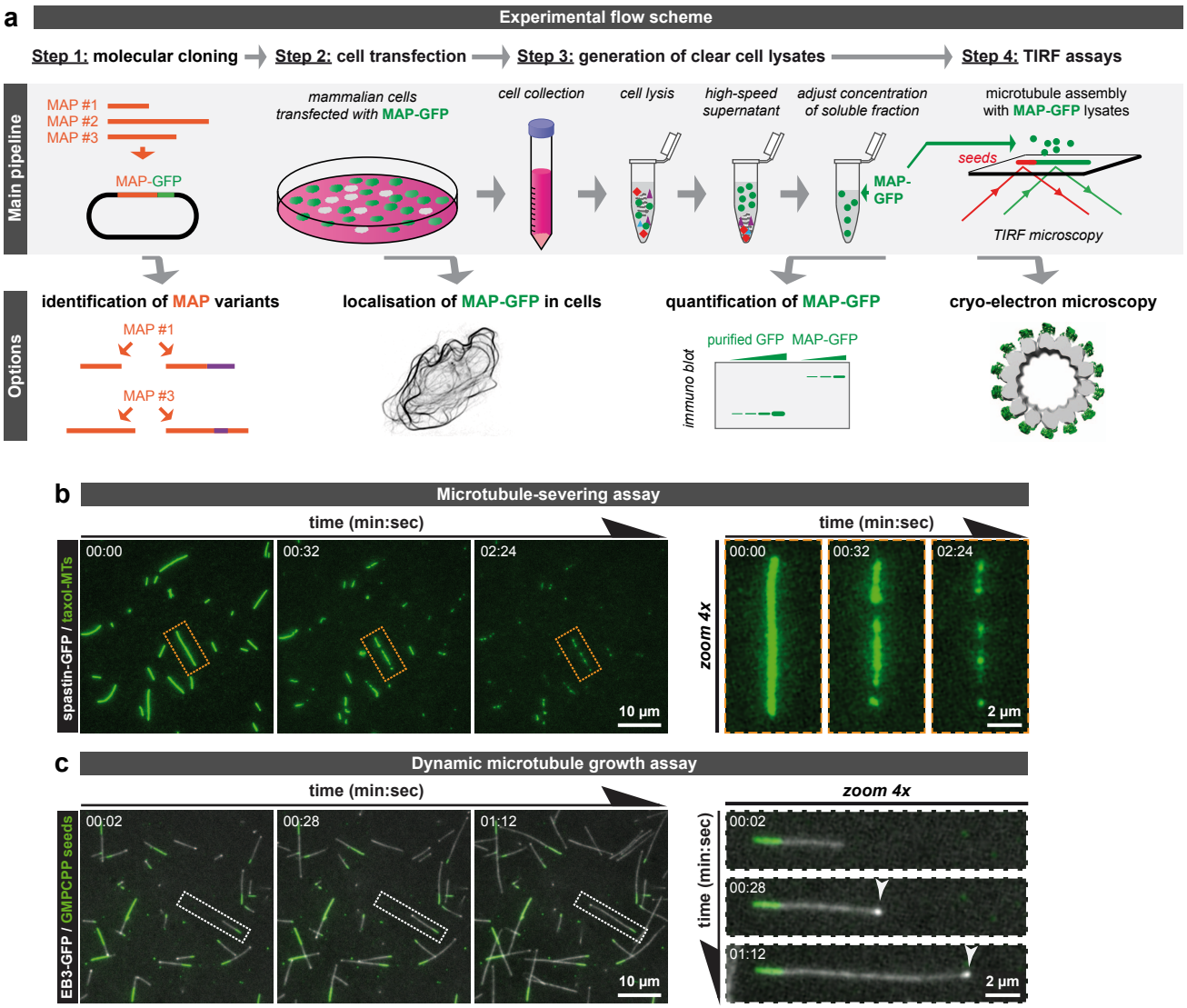
a
Experimental flow scheme
Step 1: molecular cloning
Step 2: cell transfection
Step 3: generation of clear cell lysates
Step 4: TIRF assays
Main pipeline
MAP #1
MAP #2
MAP #3
MAP-GFP
mammalian cells transfected with MAP-GFP
cell collection
cell lysis
high-speed supernatant
adjust concentration of soluble fraction
MAP-GFP
microtubule assembly with MAP-GFP lysates
seeds
TIRF microscopy
Options
identification of MAP variants
MAP #1
MAP #3
localisation of MAP-GFP in cells
quantification of MAP-GFP
purified GFP
MAP-GFP
immuno blot
cryo-electron microscopy
b
Microtubule-severing assay
time (min:sec)
spastin-GFP / taxol-MTs
00:00
00:32
02:24
10 µm
zoom 4x
2 µm
c
Dynamic microtubule growth assay
EB3-GFP / GMPCPP seeds
00:02
00:28
01:12
zoom 4x
time (min:sec)

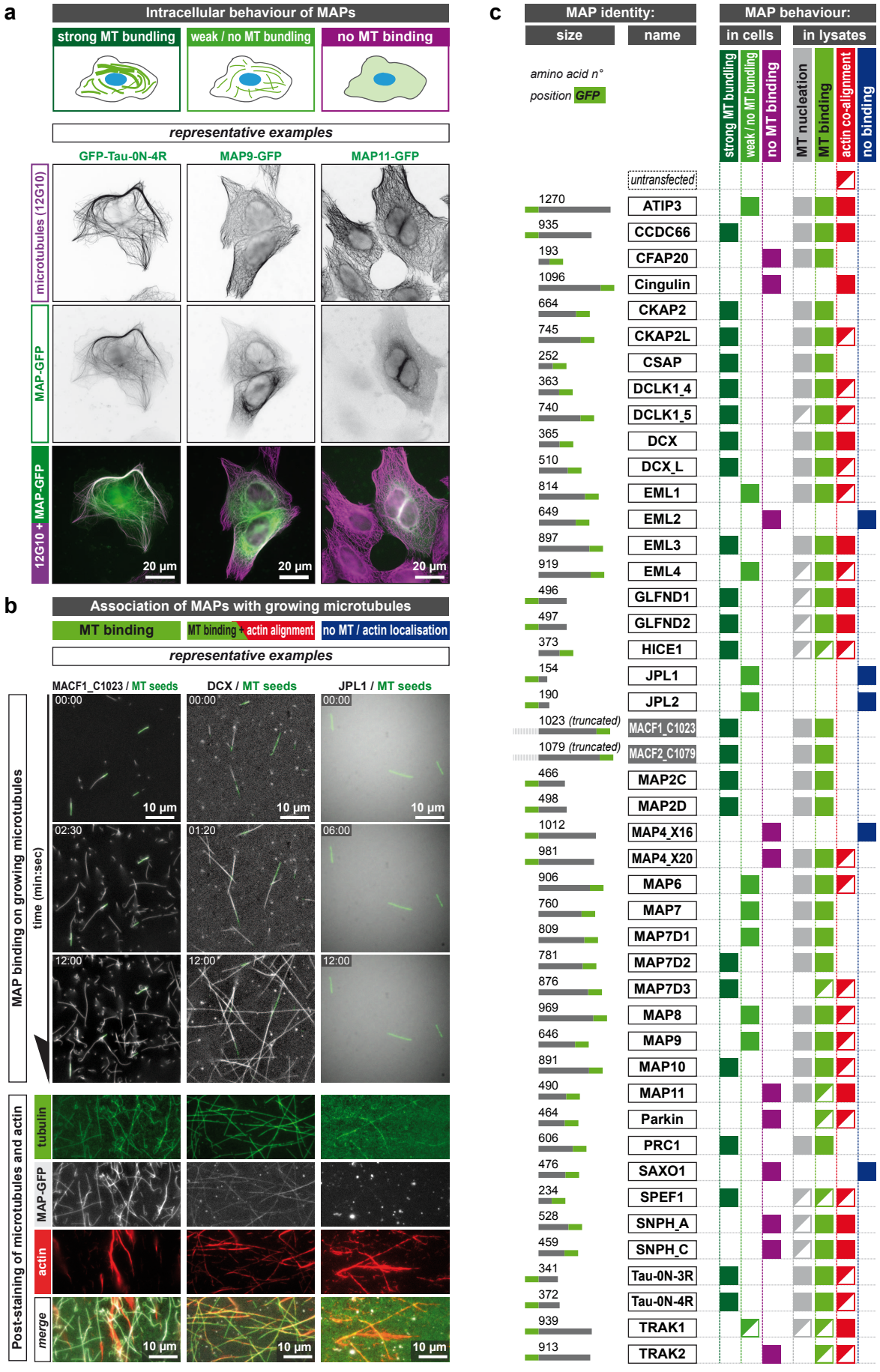
a
Intracellular behaviour of MAPs
strong MT bundling
weak / no MT bundling
no MT binding
representative examples
GFP-Tau-0N-4R
MAP9-GFP
MAP11-GFP
microtubules (12G10)
MAP-GFP
12G10 + MAP-GFP
20 µm
b
Association of MAPs with growing microtubules
MT binding
MT binding + actin alignment
no MT / actin localisation
representative examples
MACF1_C1023 / MT seeds
DCX / MT seeds
JPL1 / MT seeds
MAP binding on growing microtubules
time (min:sec)
00:00
02:30
01:20
06:00
12:00
10 µm
Post-staining of microtubules and actin
tubulin
MAP-GFP
actin
merge
c
MAP identity:
size
name
MAP behaviour:
in cells
in lysates
amino acid n°
position GFP
strong MT bundling
weak / no MT bundling
no MT binding
MT nucleation
MT binding
actin co-alignment
no binding
untransfected
1270 ATIP3
935 CCDC66
193 CFAP20
1096 Cingulin
664 CKAP2
745 CKAP2L
252 CSAP
363 DCLK1_4
740 DCLK1_5
365 DCX
510 DCX_L
814 EML1
649 EML2
897 EML3
919 EML4
496 GLFND1
497 GLFND2
373 HICE1
154 JPL1
190 JPL2
1023 (truncated) MACF1_C1023
1079 (truncated) MACF2_C1079
466 MAP2C
498 MAP2D
1012 MAP4_X16
981 MAP4_X20
906 MAP6
760 MAP7
809 MAP7D1
781 MAP7D2
876 MAP7D3
969 MAP8
646 MAP9
891 MAP10
490 MAP11
464 Parkin
606 PRC1
476 SAXO1
234 SPEF1
528 SNPH_A
459 SNPH_C
341 Tau-0N-3R
372 Tau-0N-4R
939 TRAK1
913 TRAK2

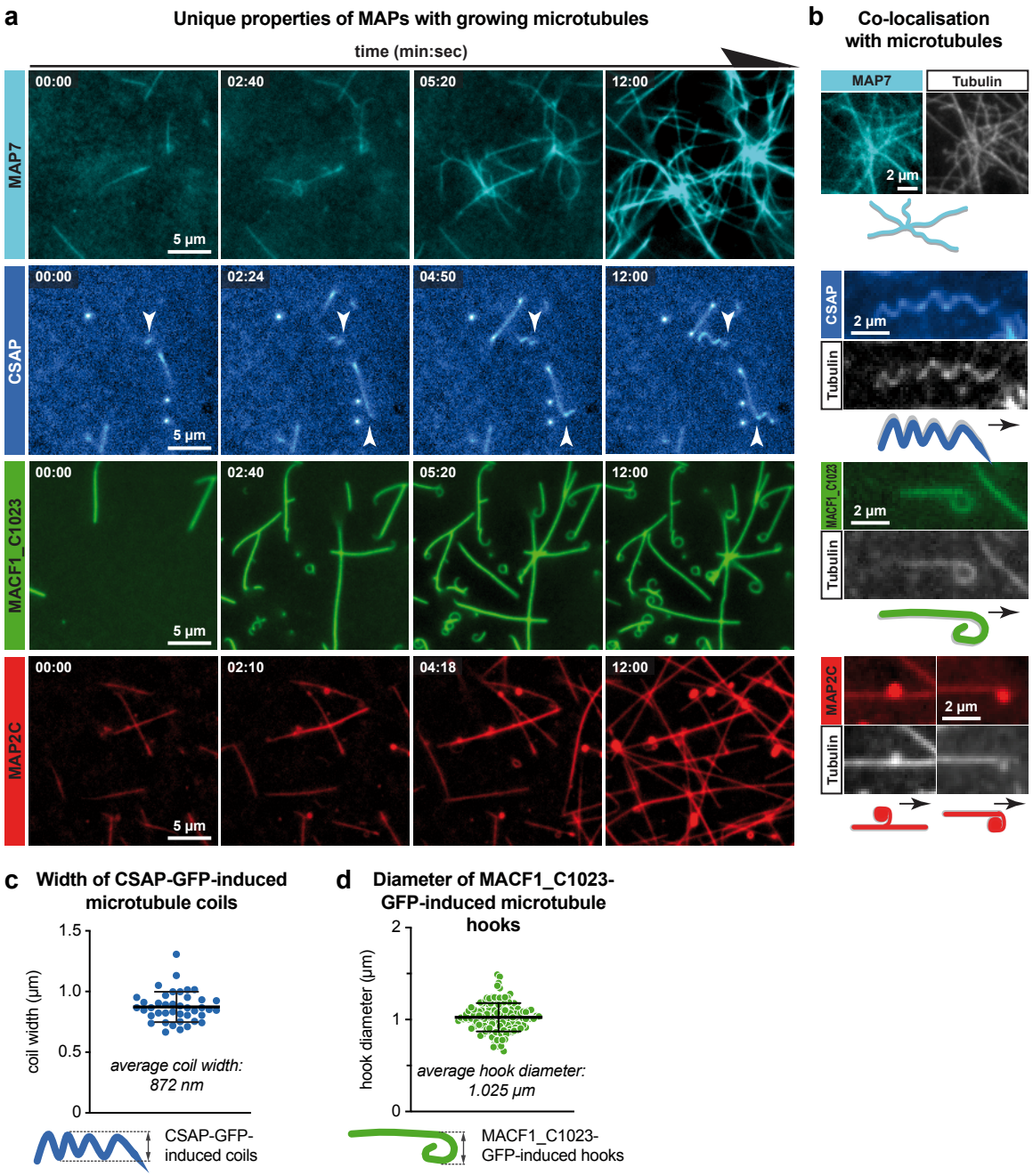
a
Unique properties of MAPs with growing microtubules
time (min:sec)
MAP7
CSAP
MACF1_C1023
MAP2C
00:00
02:40
05:20
12:00
02:24
04:50
02:10
04:18
5 µm
b
Co-localisation with microtubules
MAP7
Tubulin
2 µm
CSAP
MACF1_C1023
MAP2C
c
Width of CSAP-GFP-induced microtubule coils
coil width (µm)
1.5
1.0
0.5
0
average coil width: 872 nm
CSAP-GFP-induced coils
d
Diameter of MACF1_C1023-GFP-induced microtubule hooks
hook diameter (µm)
2
1
0
average hook diameter: 1.025 µm
MACF1_C1023-GFP-induced hooks

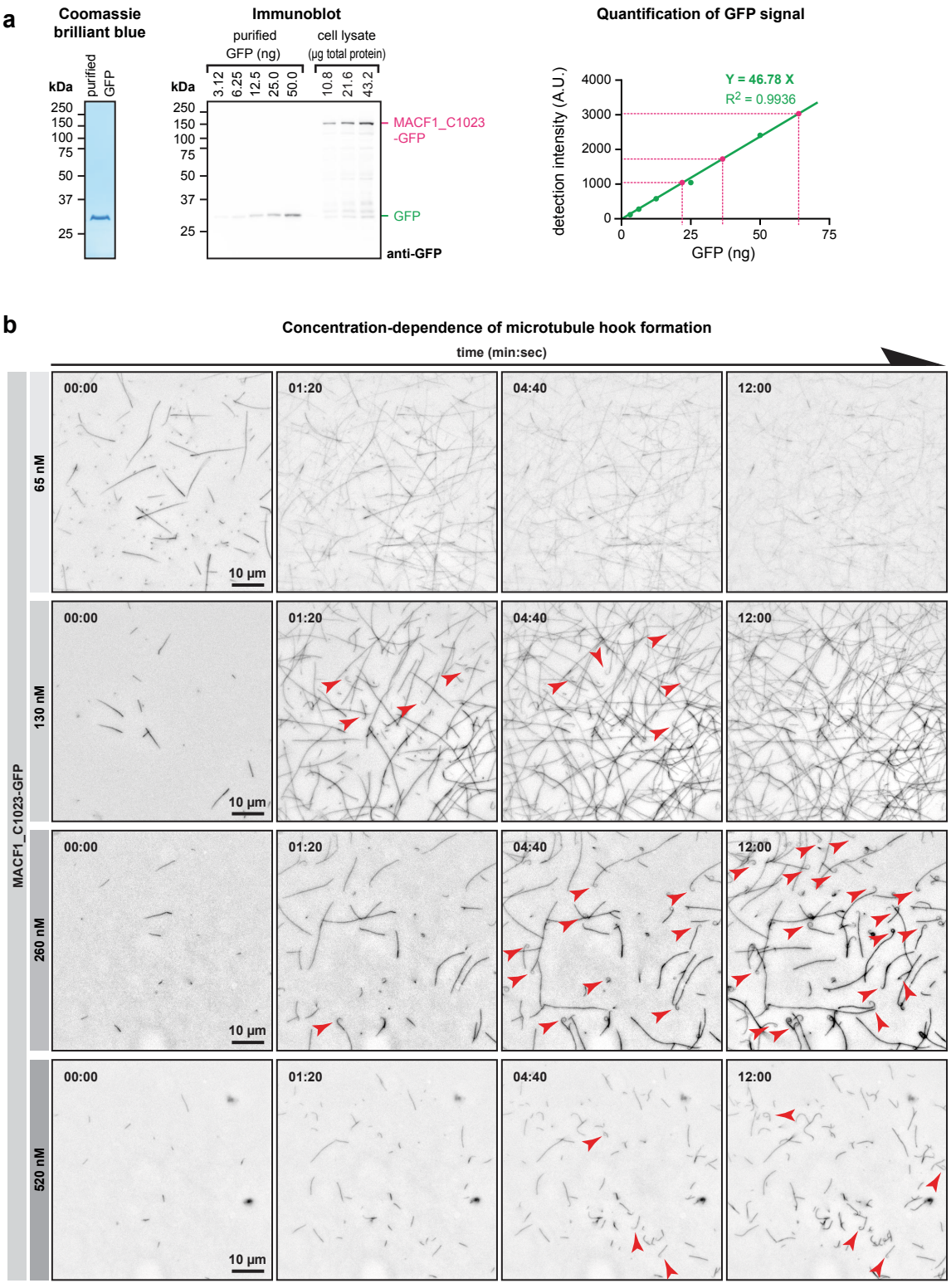
a
Coomassie brilliant blue
kDa
purified GFP
250
150
100
75
50
37
25
Immunoblot
purified GFP (ng)
cell lysate (µg total protein)
kDa
3.12
6.25
12.5
25.0
50.0
10.8
21.6
43.2
250
150
100
75
50
37
25
MACF1_C1023 -GFP
GFP
anti-GFP
Quantification of GFP signal
detection intensity (A.U.)
4000
3000
2000
1000
0
Y = 46.78 X
R2 = 0.9936
0
25
50
75
GFP (ng)
b
Concentration-dependence of microtubule hook formation
time (min:sec)
MACF1_C1023-GFP
65 nM
130 nM
260 nM
520 nM
00:00
01:20
04:40
12:00
10 µm

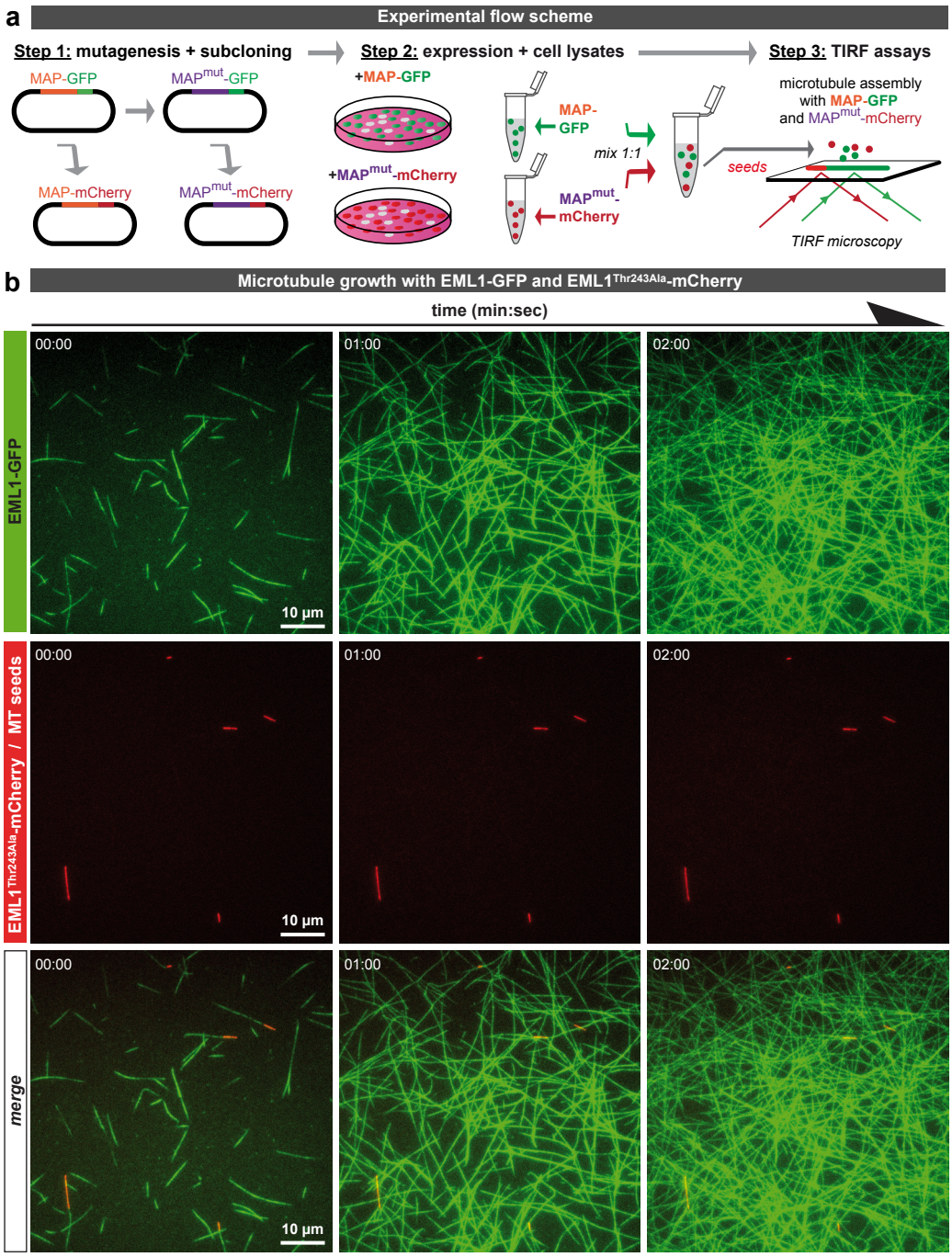
a
Experimental flow scheme
Step 1: mutagenesis + subcloning
Step 2: expression + cell lysates
Step 3: TIRF assays
MAP-GFP
MAPmut-GFP
MAP-mCherry
MAPmut-mCherry
+MAP-GFP
+MAPmut-mCherry
MAP-GFP
MAPmut-mCherry
mix 1:1
seeds
microtubule assembly with MAP-GFP and MAPmut-mCherry
TIRF microscopy
b
Microtubule growth with EML1-GFP and EML1Thr243Ala-mCherry
time (min:sec)
EML1-GFP
EML1Thr243Ala-mCherry / MT seeds
merge
00:00
01:00
02:00
10 µm

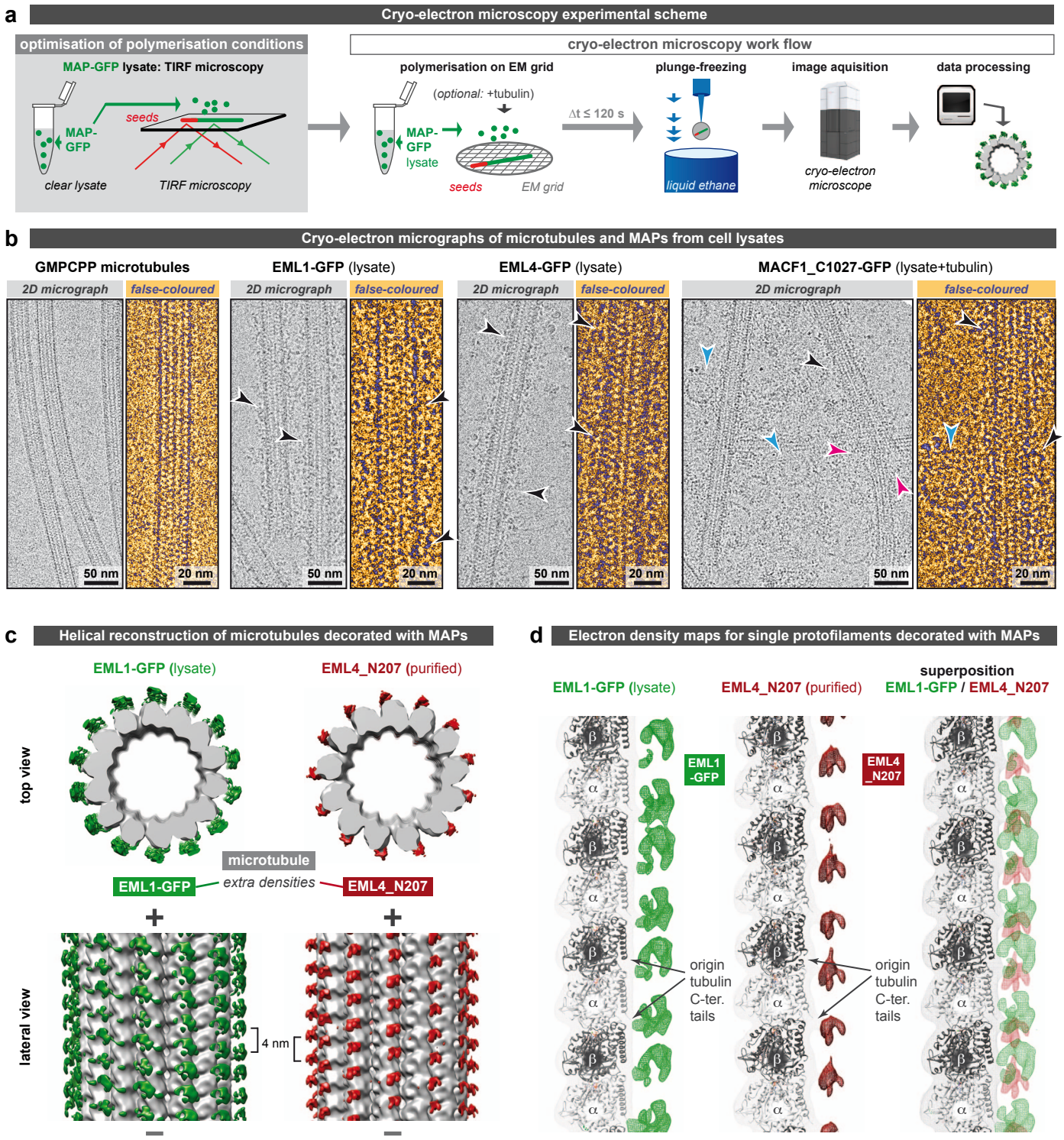
a
Cryo-electron microscopy experimental scheme
optimisation of polymerisation conditions
MAP-GFP lysate: TIRF microscopy
MAP-GFP
seeds
clear lysate
TIRF microscopy
cryo-electron microscopy work flow
polymerisation on EM grid
(optional: +tubulin)
MAP-GFP lysate
seeds
EM grid
Δt ≤ 120 s
plunge-freezing
liquid ethane
image aquisition
cryo-electron microscope
data processing
b
Cryo-electron micrographs of microtubules and MAPs from cell lysates
GMPCPP microtubules
EML1-GFP (lysate)
EML4-GFP (lysate)
MACF1_C1027-GFP (lysate+tubulin)
2D micrograph
false-coloured
50 nm
20 nm
c
Helical reconstruction of microtubules decorated with MAPs
EML1-GFP (lysate)
EML4_N207 (purified)
top view
microtubule
EML1-GFP
extra densities
EML4_N207
lateral view
4 nm
d
Electron density maps for single protofilaments decorated with MAPs
EML1-GFP (lysate)
EML4_N207 (purified)
superposition
EML1-GFP / EML4_N207
EML1-GFP
EML4_N207
origin tubulin C-ter. tails
β
α

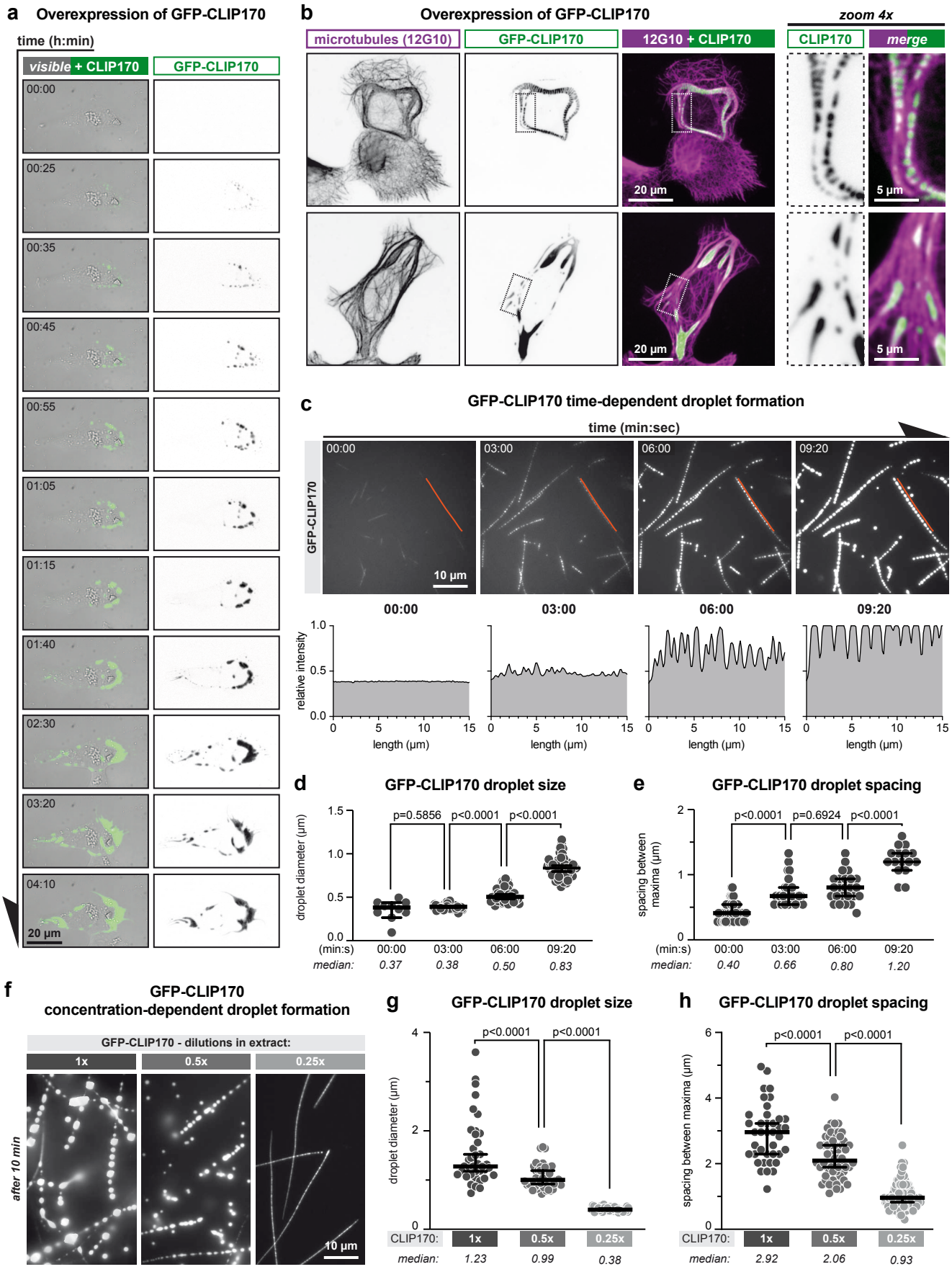
a
Overexpression of GFP-CLIP170
time (h:min)
visible + CLIP170
GFP-CLIP170
00:00
00:25
00:35
00:45
00:55
01:05
01:15
01:40
02:30
03:20
04:10
20 µm
b
Overexpression of GFP-CLIP170
zoom 4x
microtubules (12G10)
GFP-CLIP170
12G10 + CLIP170
CLIP170
merge
20 µm
5 µm
c
GFP-CLIP170 time-dependent droplet formation
time (min:sec)
GFP-CLIP170
00:00
03:00
06:00
09:20
10 µm
relative intensity
length (µm)
d
GFP-CLIP170 droplet size
droplet diameter (µm)
p=0.5856
p<0.0001
p<0.0001
(min:s)
median:
0.37
0.38
0.50
0.83
e
GFP-CLIP170 droplet spacing
spacing between maxima (µm)
p<0.0001
p=0.6924
p<0.0001
median:
0.40
0.66
0.80
1.20
f
GFP-CLIP170
concentration-dependent droplet formation
GFP-CLIP170 - dilutions in extract:
1x
0.5x
0.25x
after 10 min
10 µm
g
GFP-CLIP170 droplet size
droplet diameter (µm)
p<0.0001
p<0.0001
CLIP170:
median:
1.23
0.99
0.38
h
GFP-CLIP170 droplet spacing
spacing between maxima (µm)
p<0.0001
p<0.0001
CLIP170:
median:
2.92
2.06
0.93

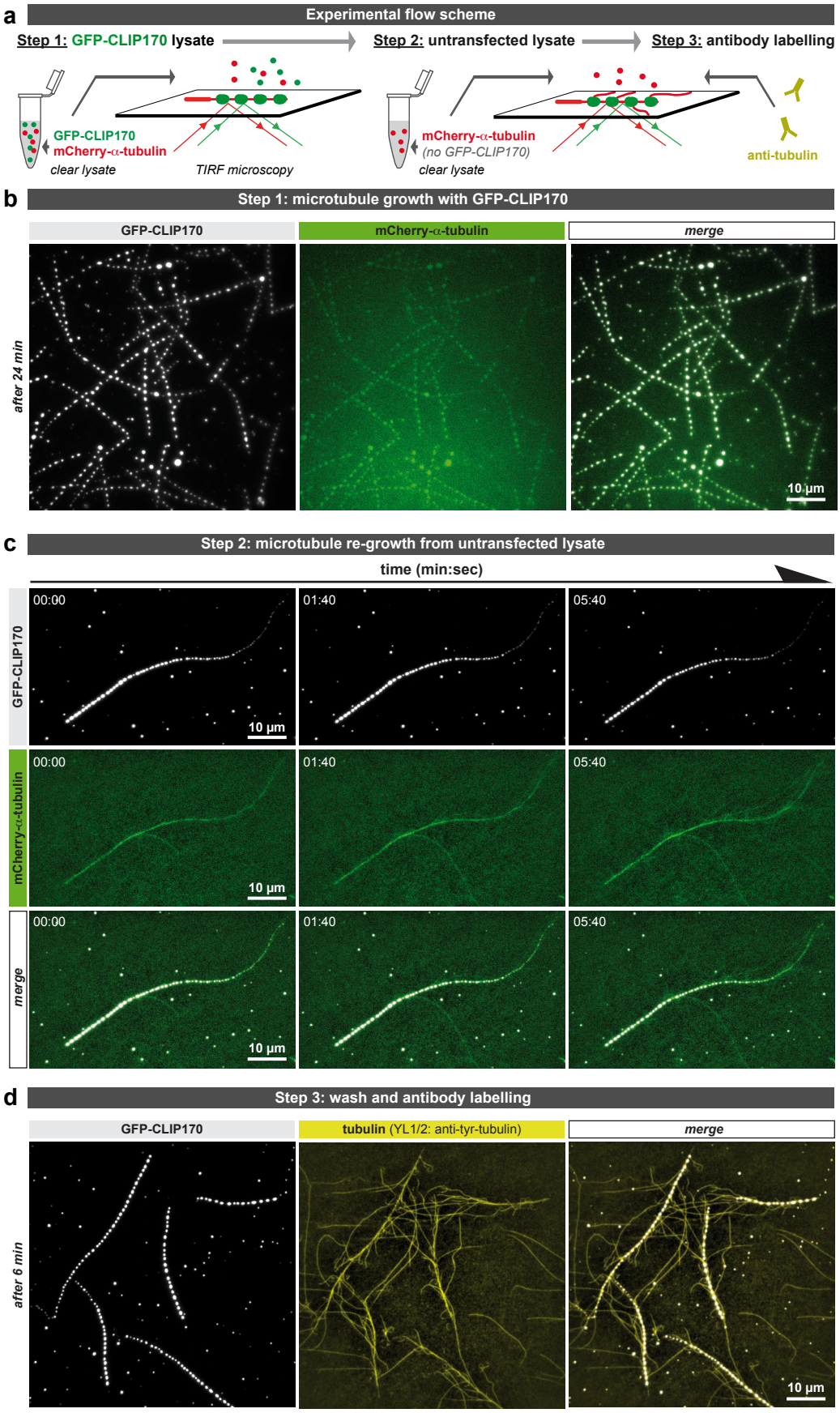
a
Experimental flow scheme
Step 1: GFP-CLIP170 lysate
Step 2: untransfected lysate
Step 3: antibody labelling
GFP-CLIP170
mCherry-α-tubulin
clear lysate
TIRF microscopy
mCherry-α-tubulin
(no GFP-CLIP170)
clear lysate
anti-tubulin
b
Step 1: microtubule growth with GFP-CLIP170
GFP-CLIP170
mCherry-α-tubulin
merge
after 24 min
10 µm
c
Step 2: microtubule re-growth from untransfected lysate
time (min:sec)
GFP-CLIP170
mCherry-α-tubulin
merge
00:00
01:40
05:40
10 µm
d
Step 3: wash and antibody labelling
GFP-CLIP170
tubulin (YL1/2: anti-tyr-tubulin)
merge
after 6 min
10 µm

a Cloning vector and insertion of gene of interest

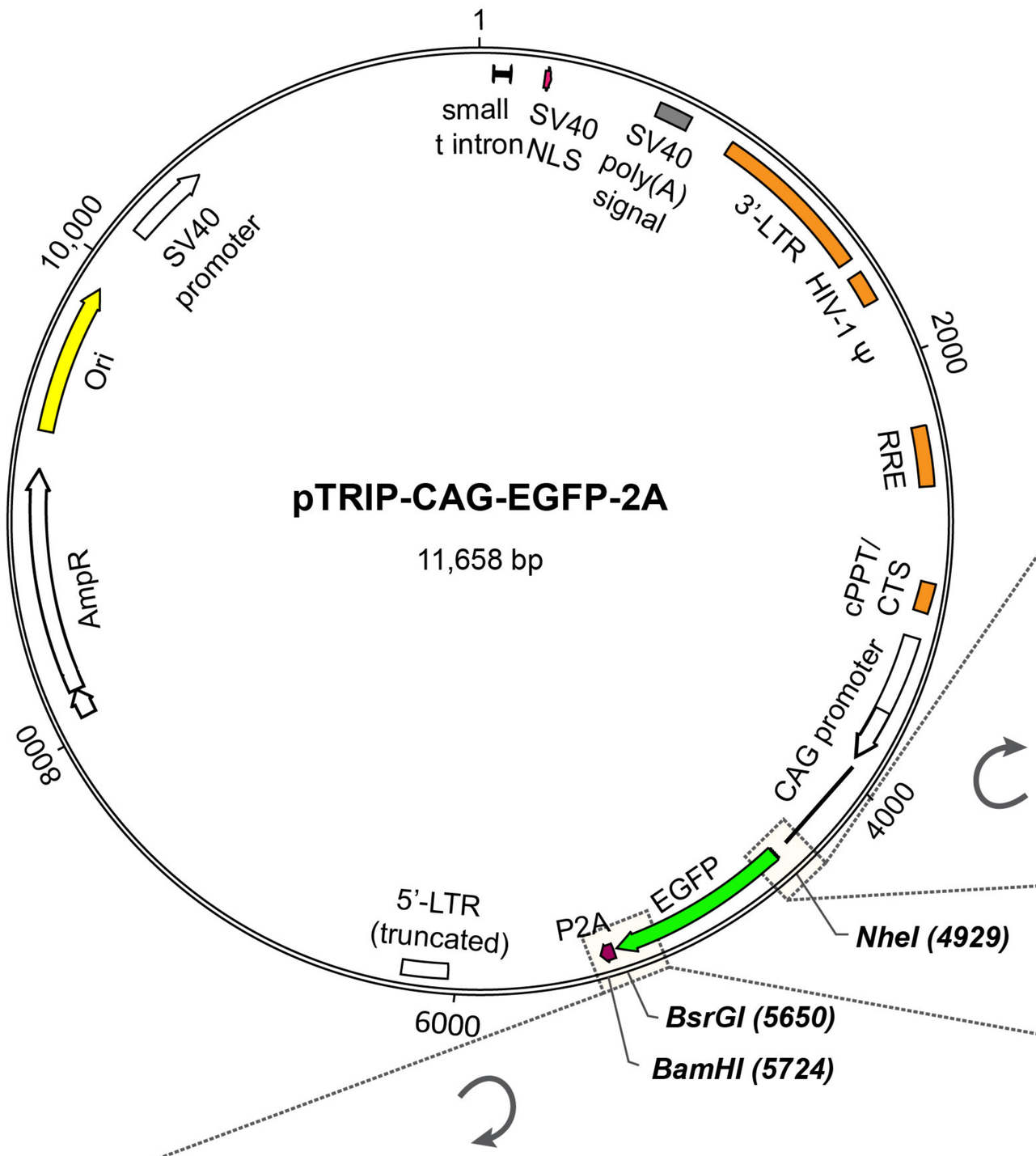

Inserting MAP before EGFP (C-terminal tag)

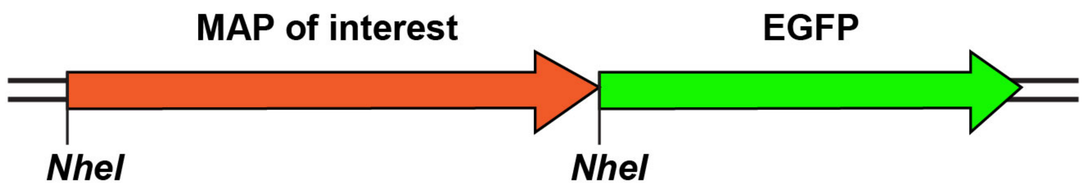

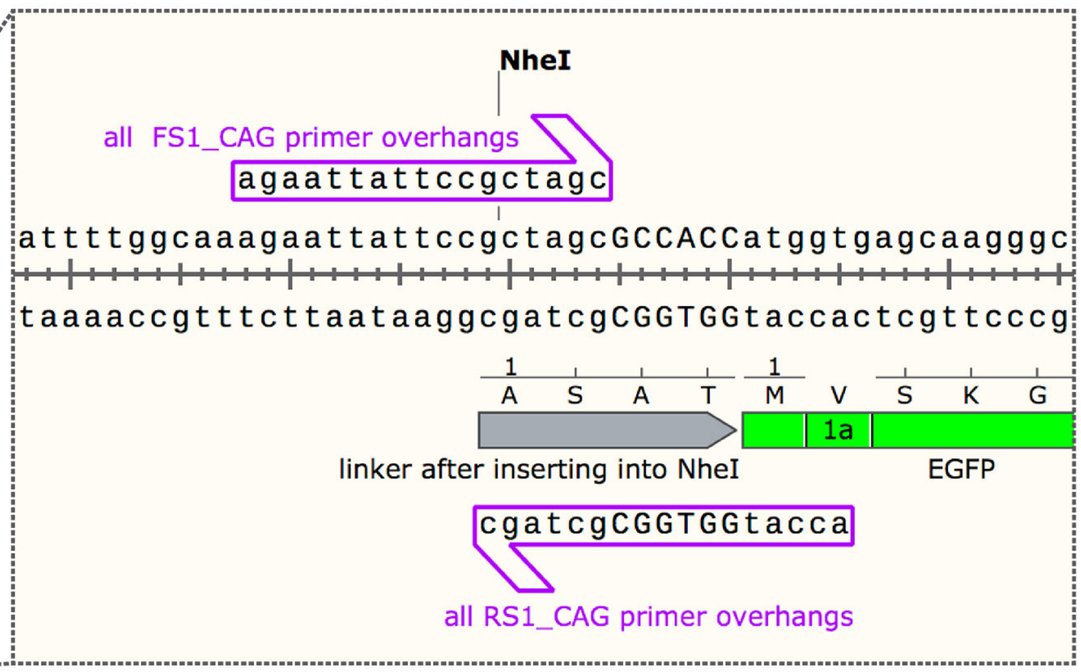

Inserting MAP after EGFP (N-terminal tag)

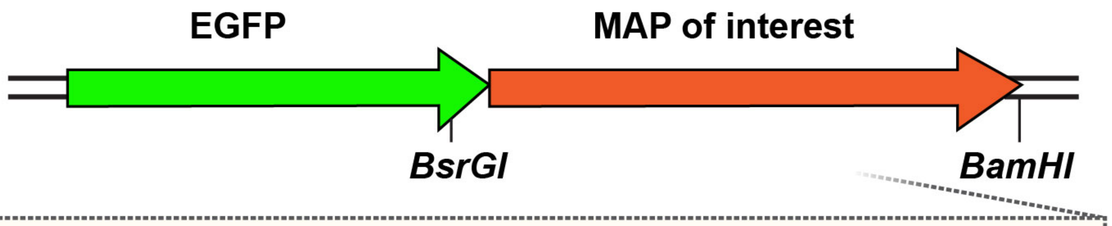

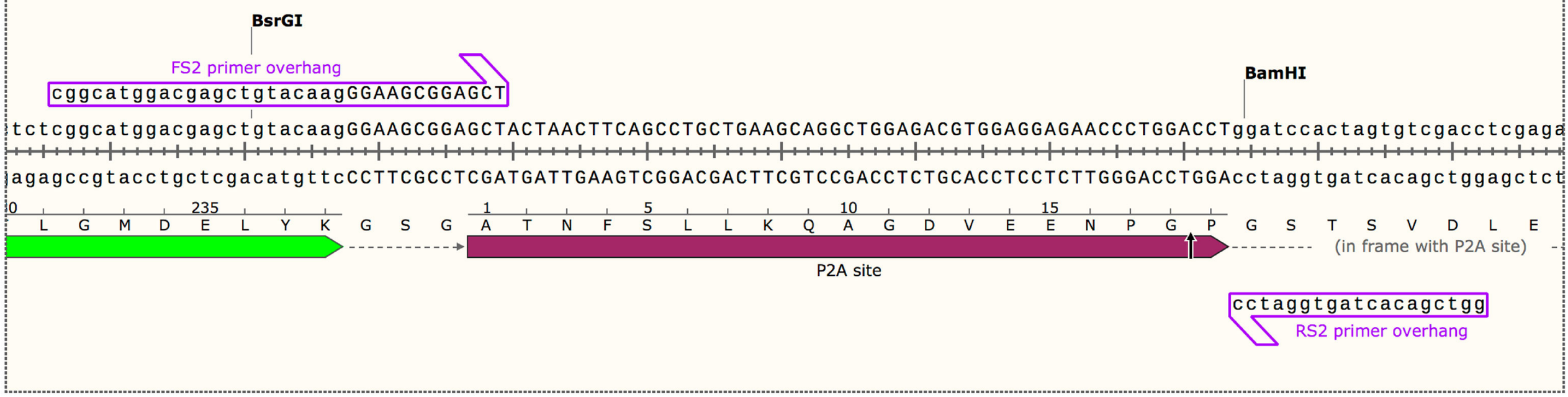

b SLIC cloning scheme

Step1: PCR-amplification of gene of interest
(with primer overhangs as indicated above)

Linearise target plasmid
(restriction enzymes as indicated above)

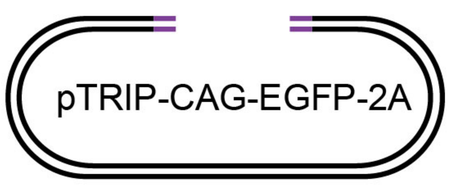

Step 2: create single-strand overhangs

T4 reaction mix (assemble at 0°C):
7 µl PCR
2 µl linearised plasmid
1 µl 10x buffer
0.2 µl T4 DNA polymerase

T4 reaction: 2.5 min, room temp.

T4: 3' exo-nuclease activity

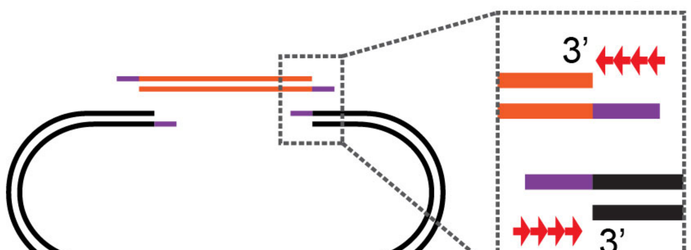

Step 3: transformation into *E. coli*
generation of plasmid-insert fusion by endogenous DNA repair mechanisms

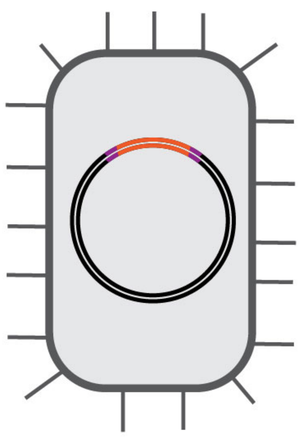

Step 4: selection

- select single colonies (6 clones)
- DNA purification
- test-digest (*NheI* or *BsrGI*/*BamHI*)
- DNA sequencing
- select clones of interest

Jijumon et al. Extended Data Figure 2

Organisation of microtubule cytoskeleton in cells with overexpressed GFP-MAPs

Jijumon et al. Extended Data Figure 3

Association of MAPs with growing microtubules

MAP binding on growing microtubules

Post-staining of microtubules and actin

time (min:sec)

tubulin | MAP-GFP | actin | *merge*

a *untransfected* / MT seeds

actin polymerisation

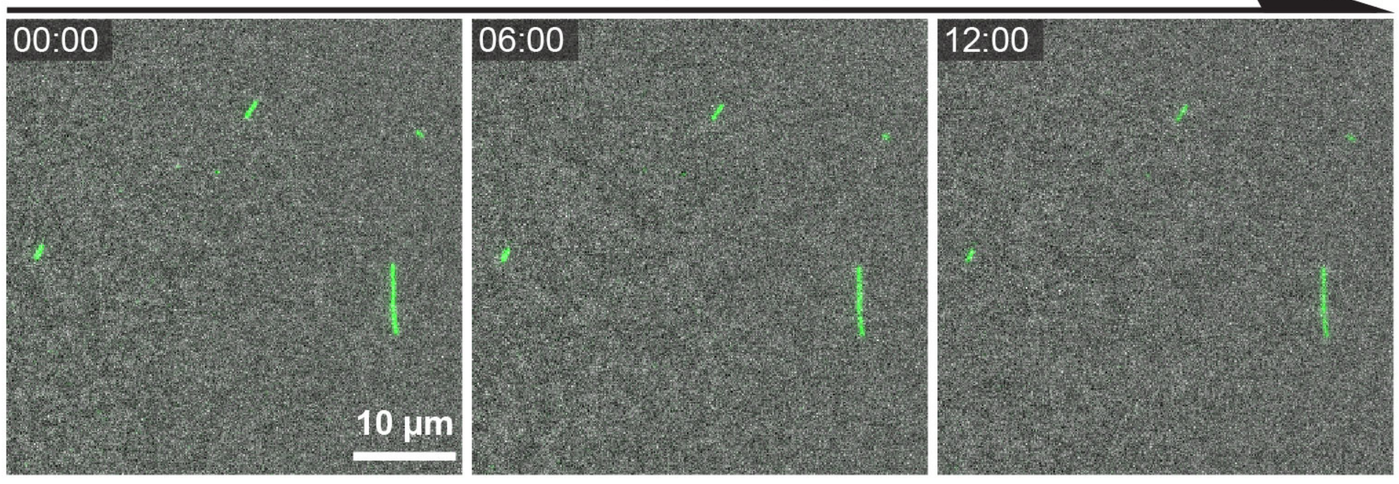

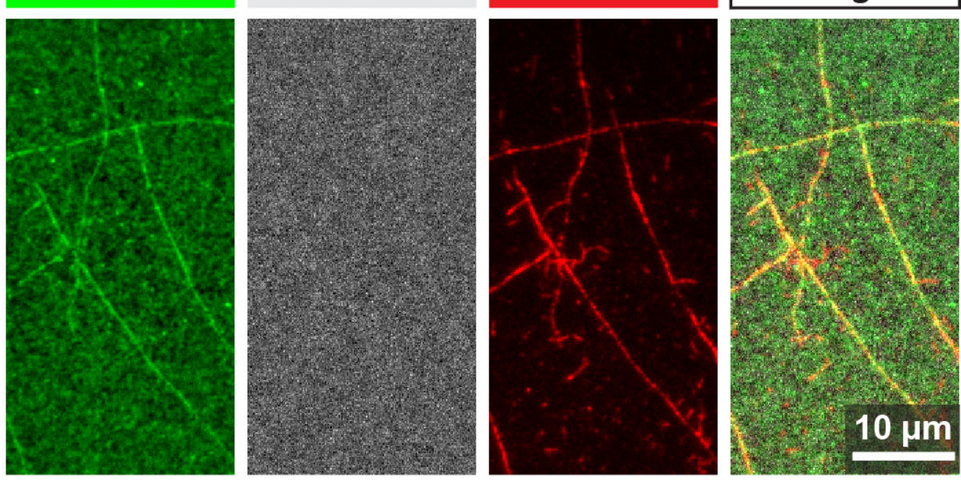

no actin polymerisation

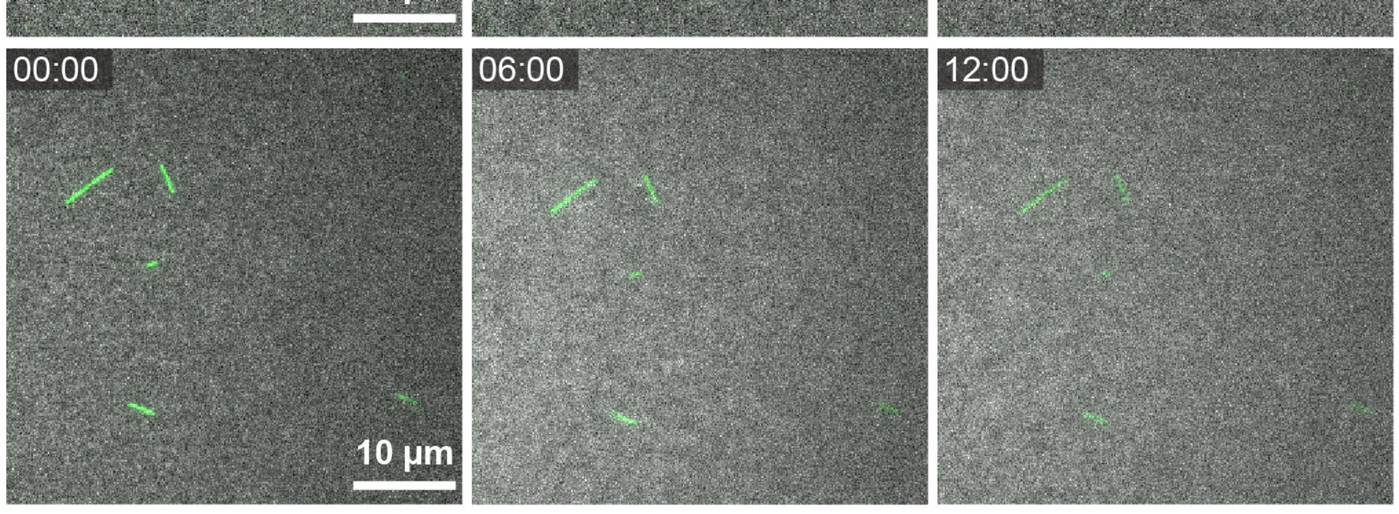

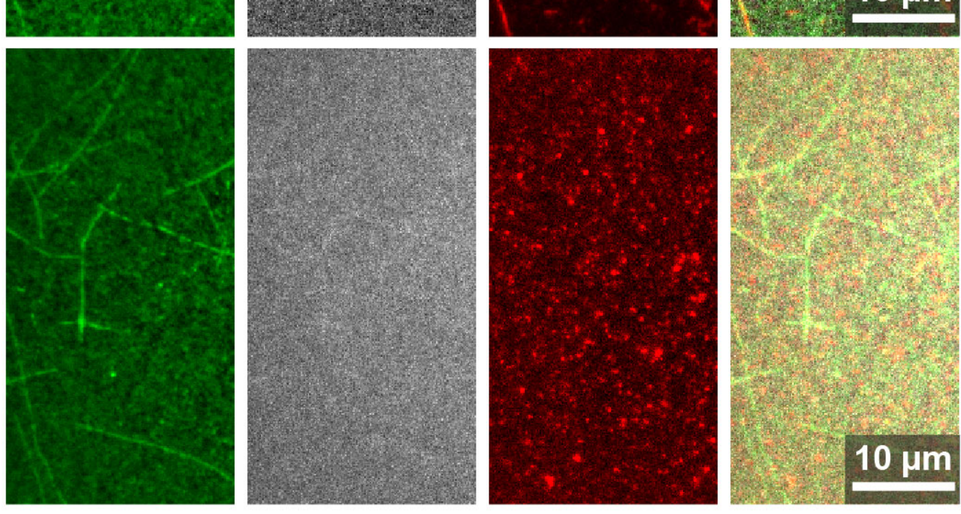

b CSAP / MT seeds

actin polymerisation

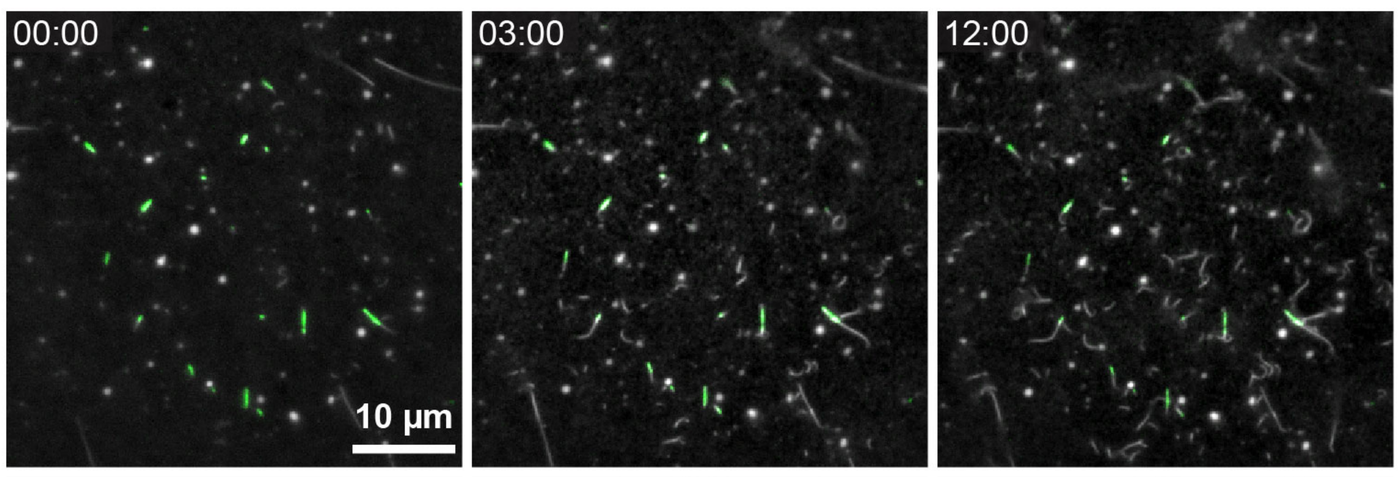

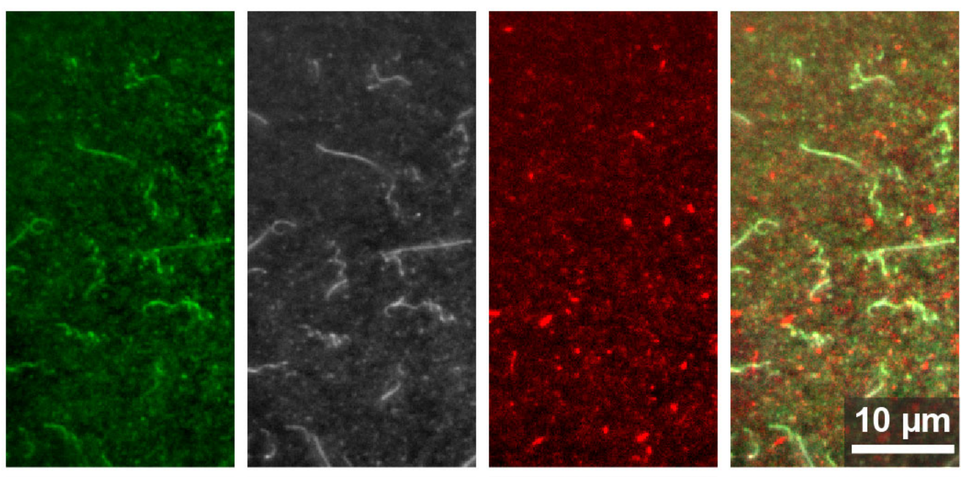

no actin polymerisation

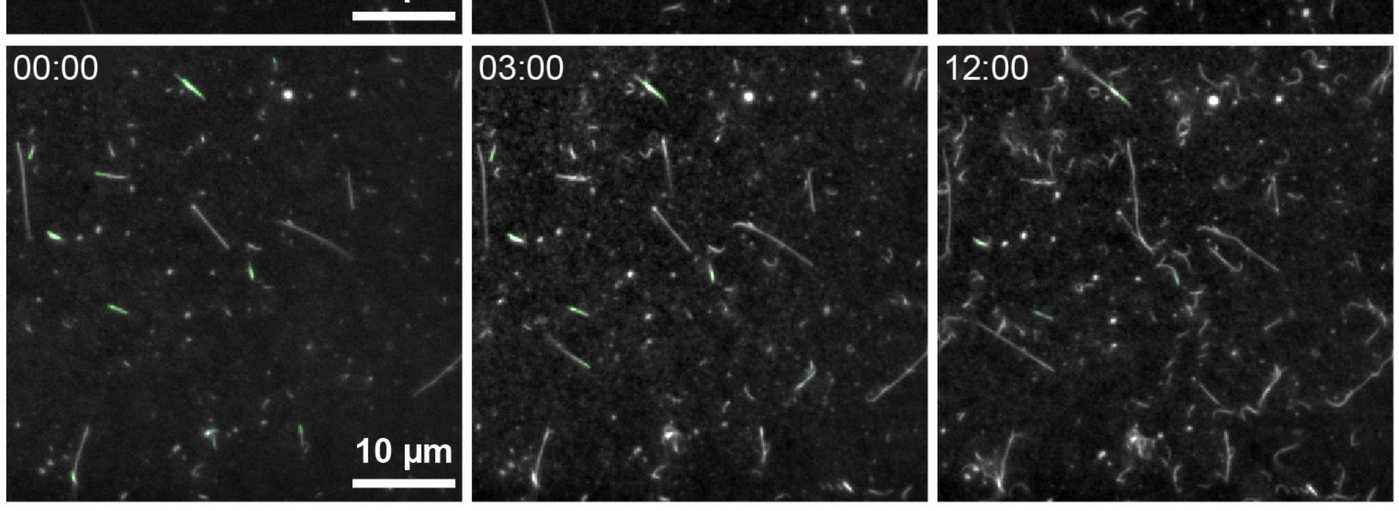

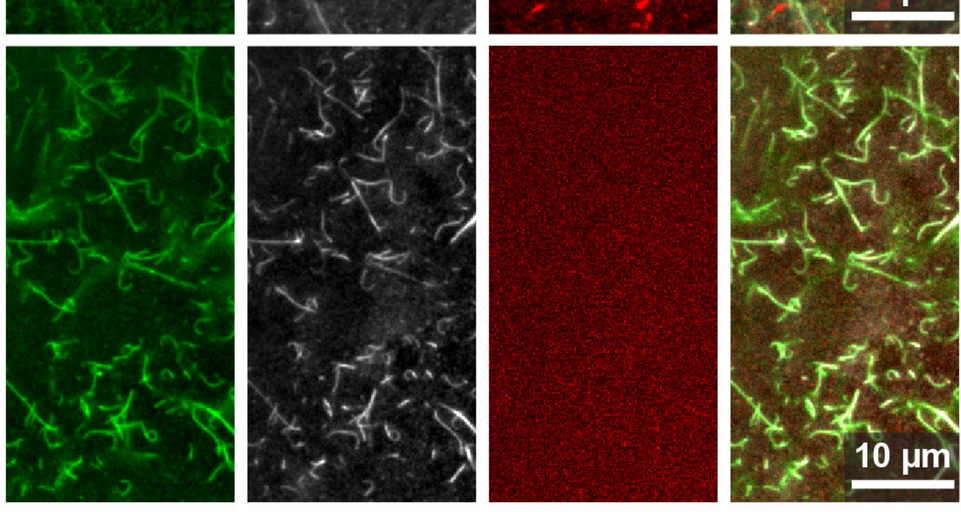

c MACF1_C1023 / MT seeds

actin polymerisation

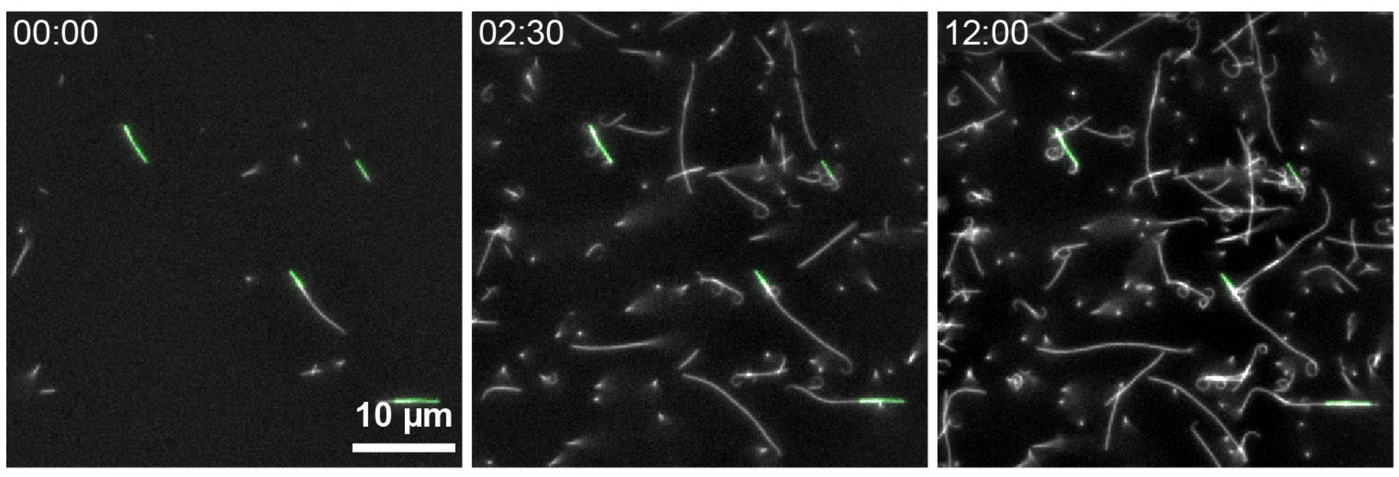

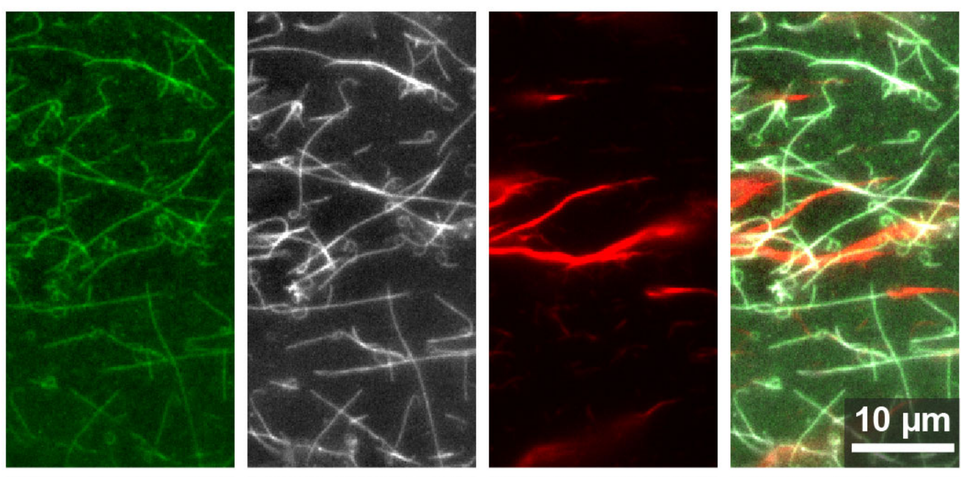

no actin polymerisation

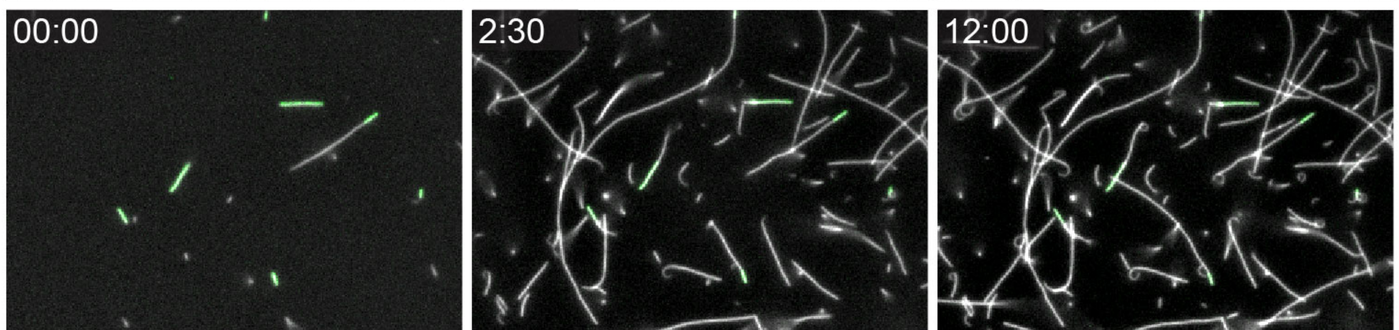

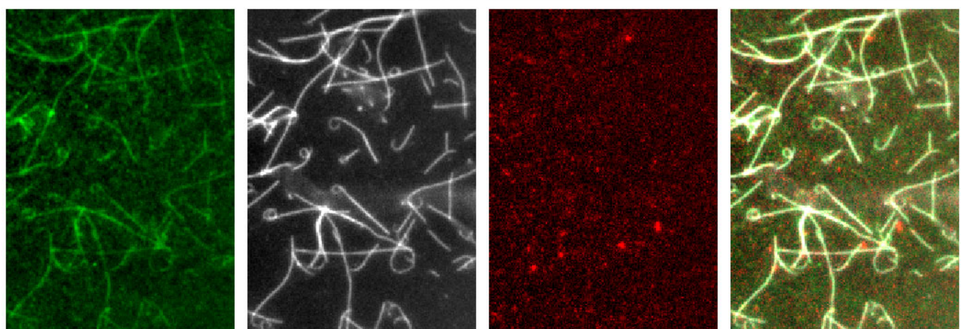

d MACF2_C1079 / MT seeds

actin polymerisation

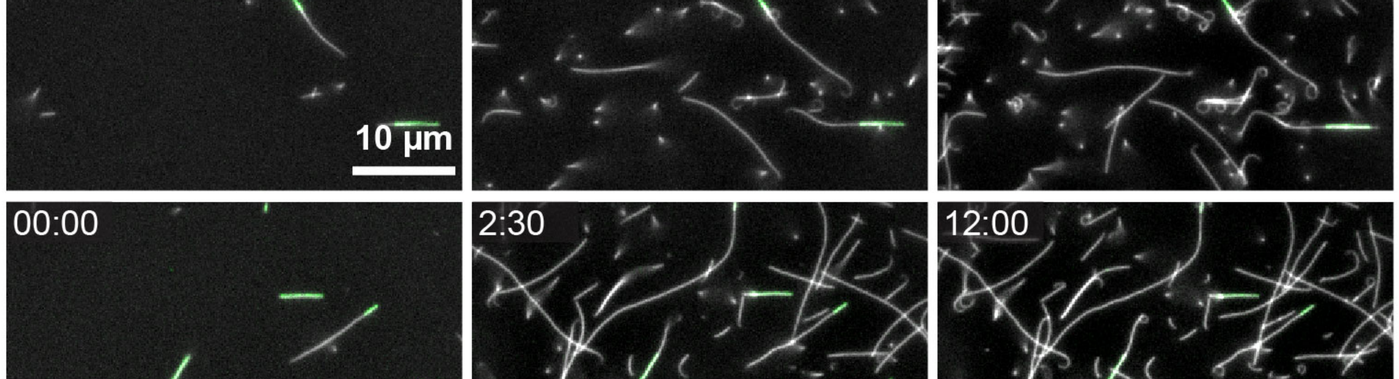

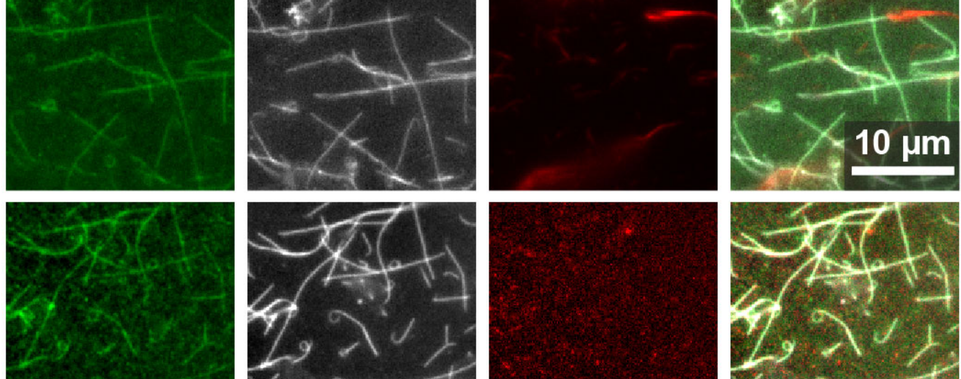

no actin polymerisation

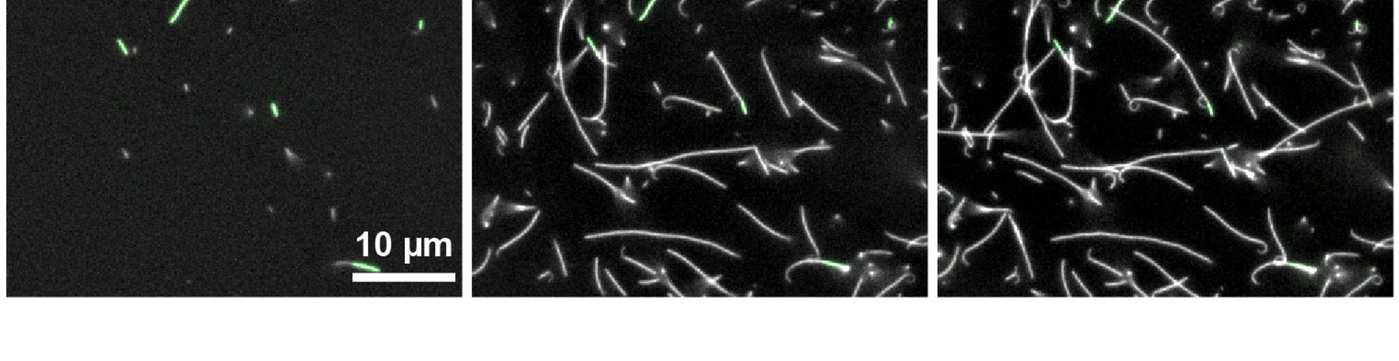

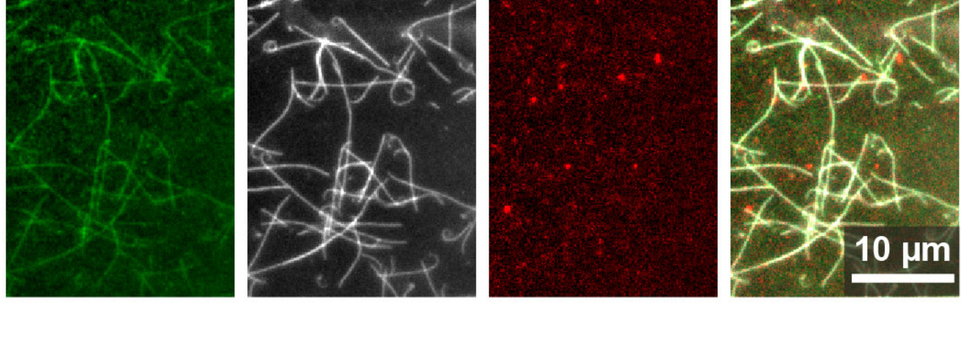

Jijumon et al. Extended Data Figure 4

Association of MAPs with growing microtubules

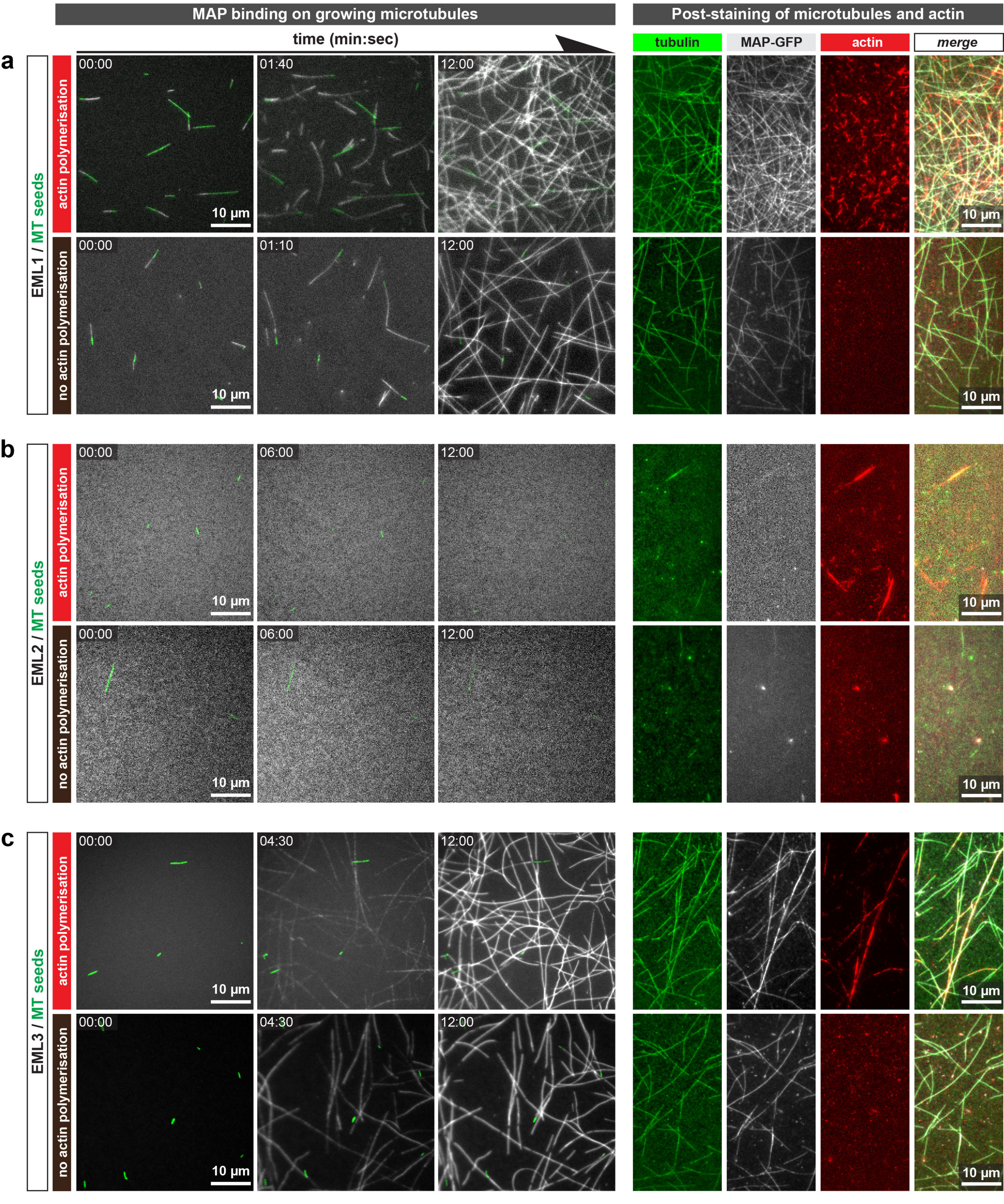

Jijumon et al. Extended Data Figure 5

Association of MAPs with growing microtubules

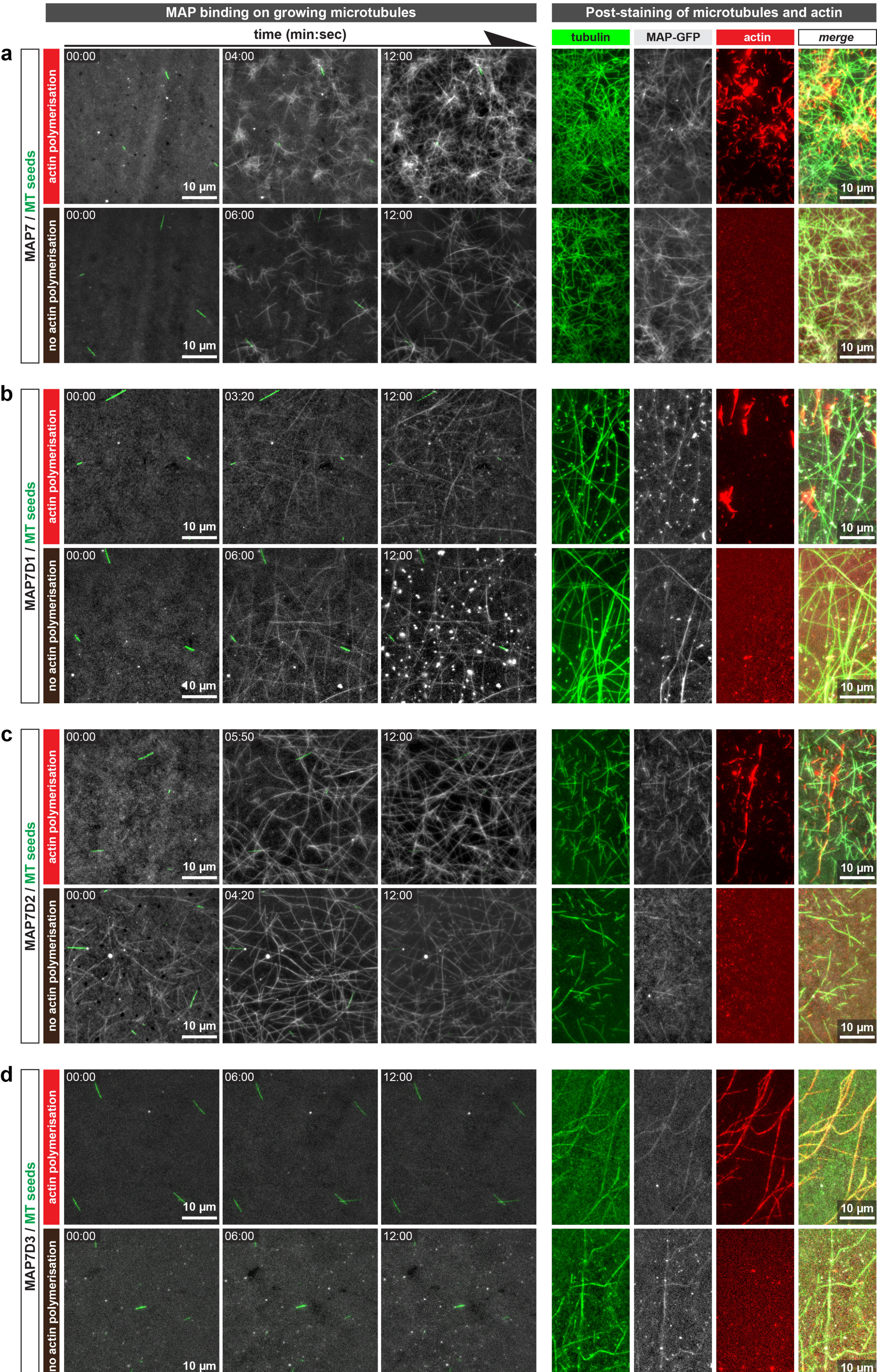

Jijumon et al. Extended Data Figure 6

Association of MAPs with growing microtubules

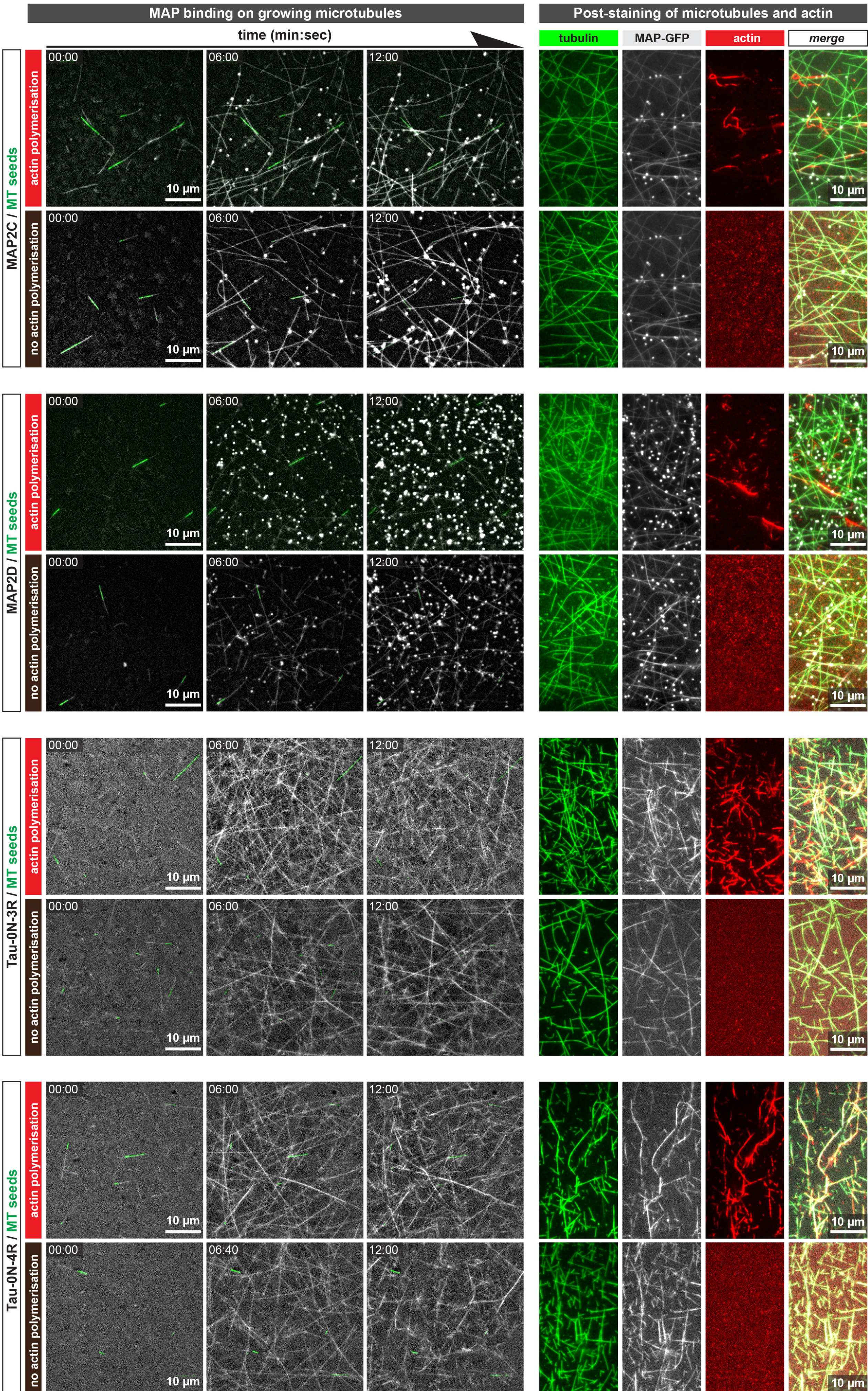

Jijumon et al. Extended Data Figure 7

a

Measurement of CSAP-GFP-induced coil width

CSAP-GFP *(after 12 min)*

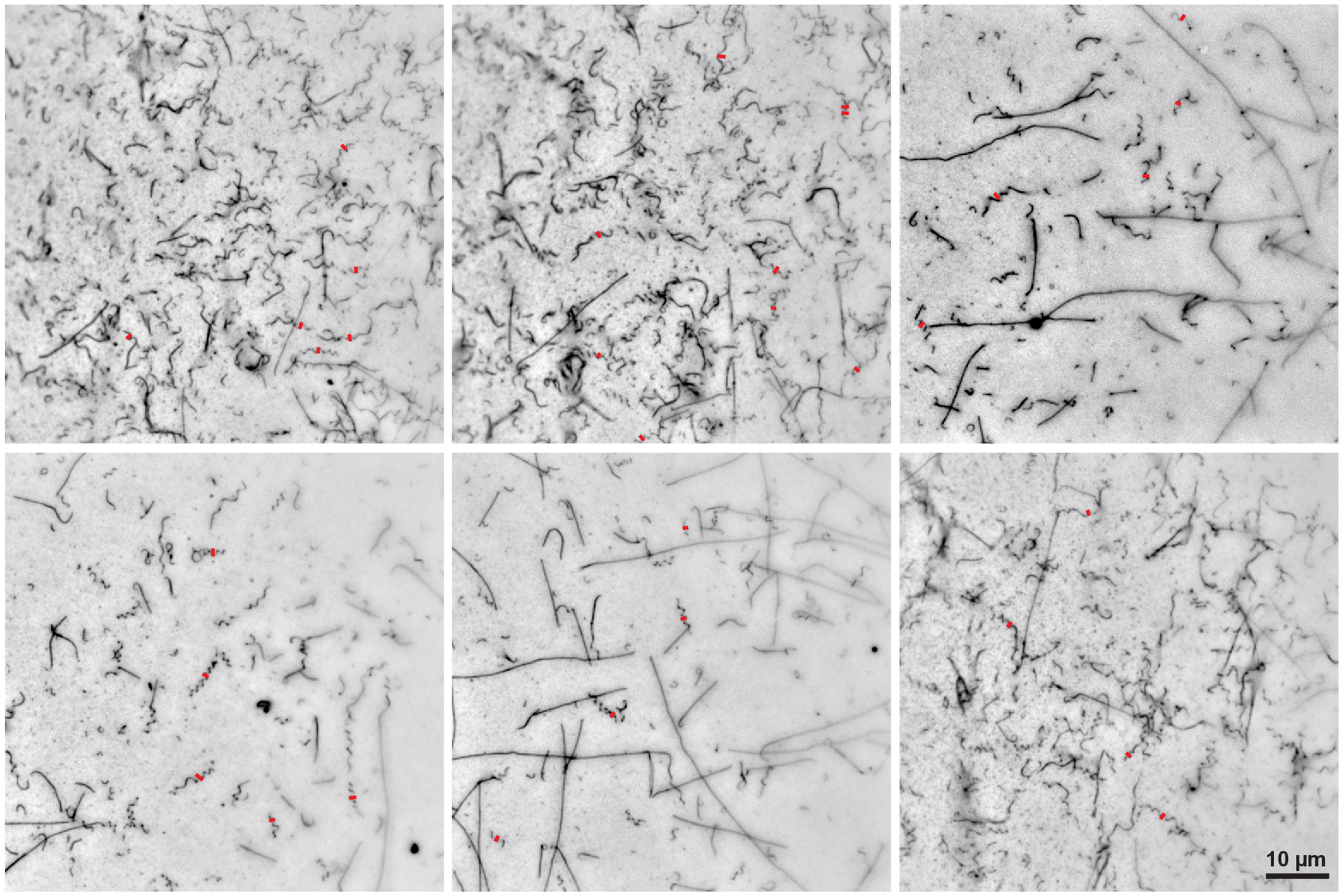

Width of microtubule coils

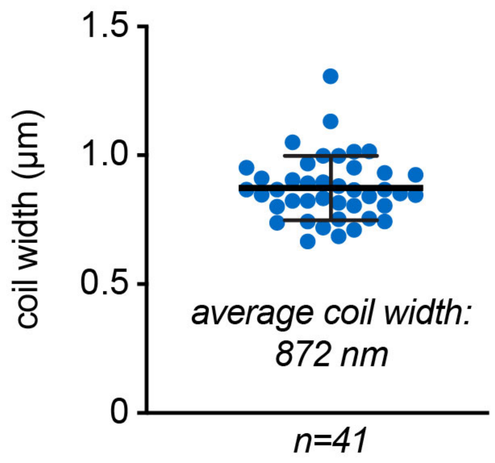

b

Measurement of MACF1_C1023-GFP-induced hook diameter

MACF1_C1023-GFP *(after 12 min)*

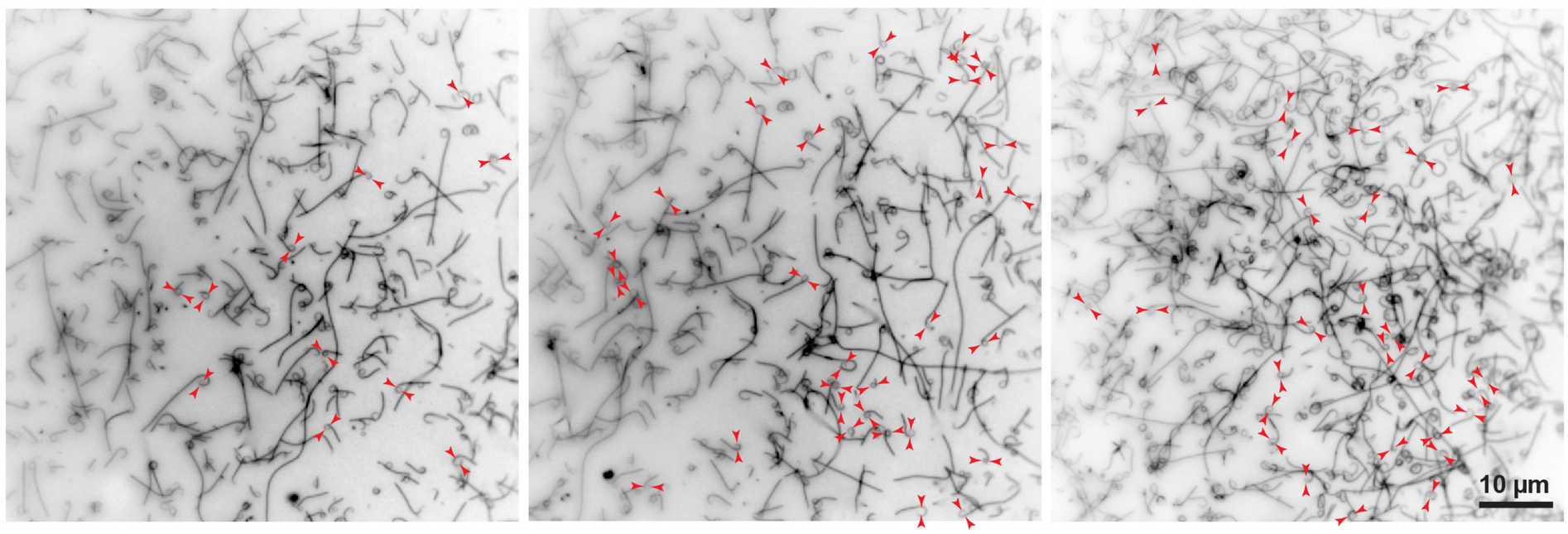

Diameter of microtubule hooks

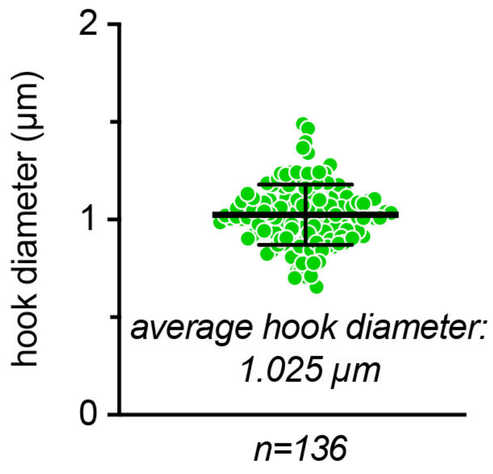

c

GFP-MAP2C

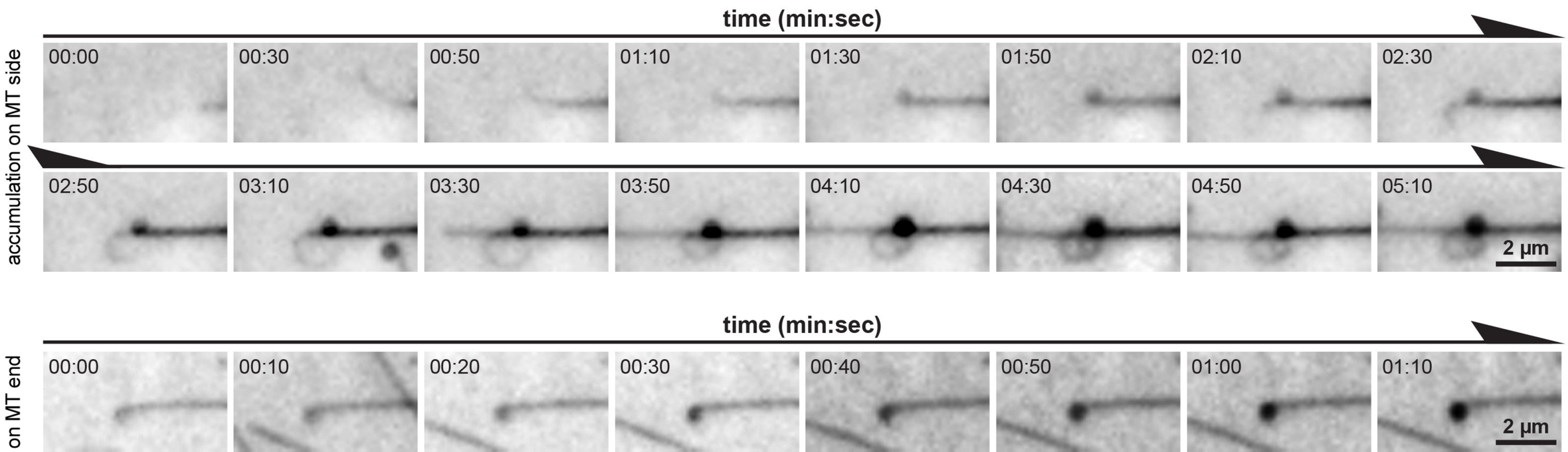

Jijumon et al. Extended Data Figure 8

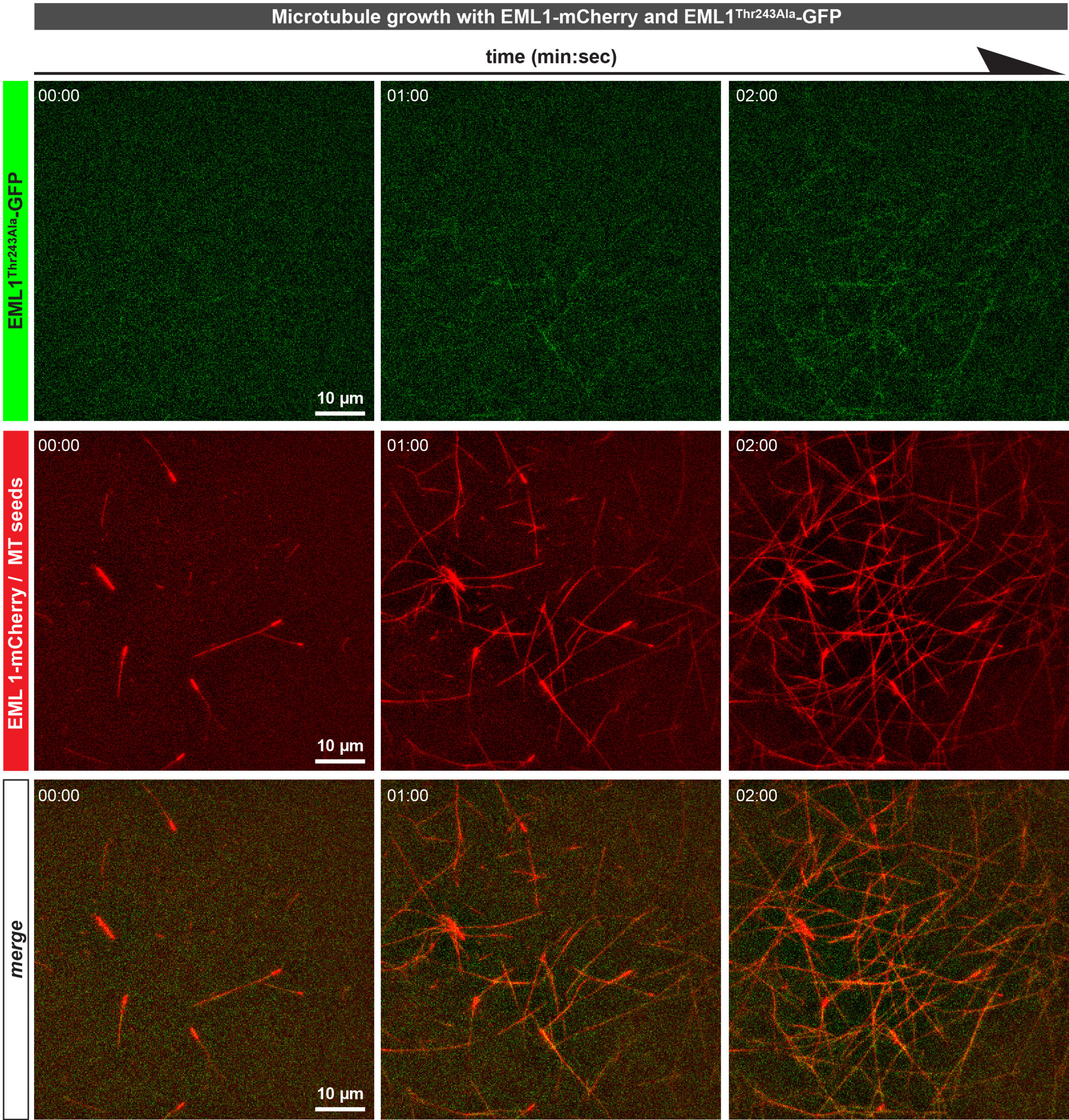

Jijumon et al. Extended Data Figure 9

a

GFP-CLIP170 droplet spacing

GFP-CLIP170 - 1x | GFP-CLIP170 - 0.5x | GFP-CLIP170 - 0.25x

after 10 min

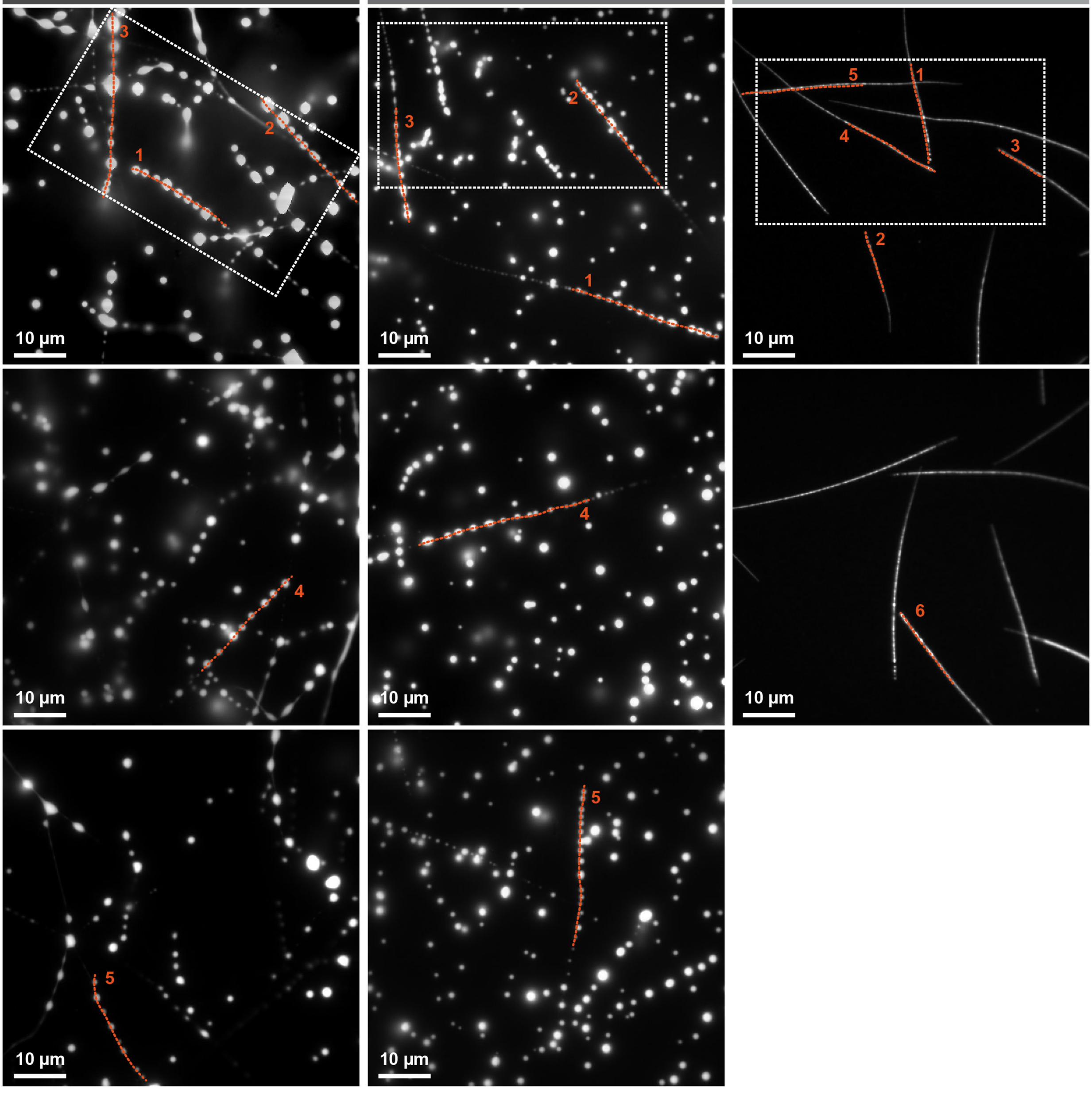

b

GFP-CLIP170 intensity profiles

GFP-CLIP170 - 1x | GFP-CLIP170 - 0.5x | GFP-CLIP170 - 0.25x

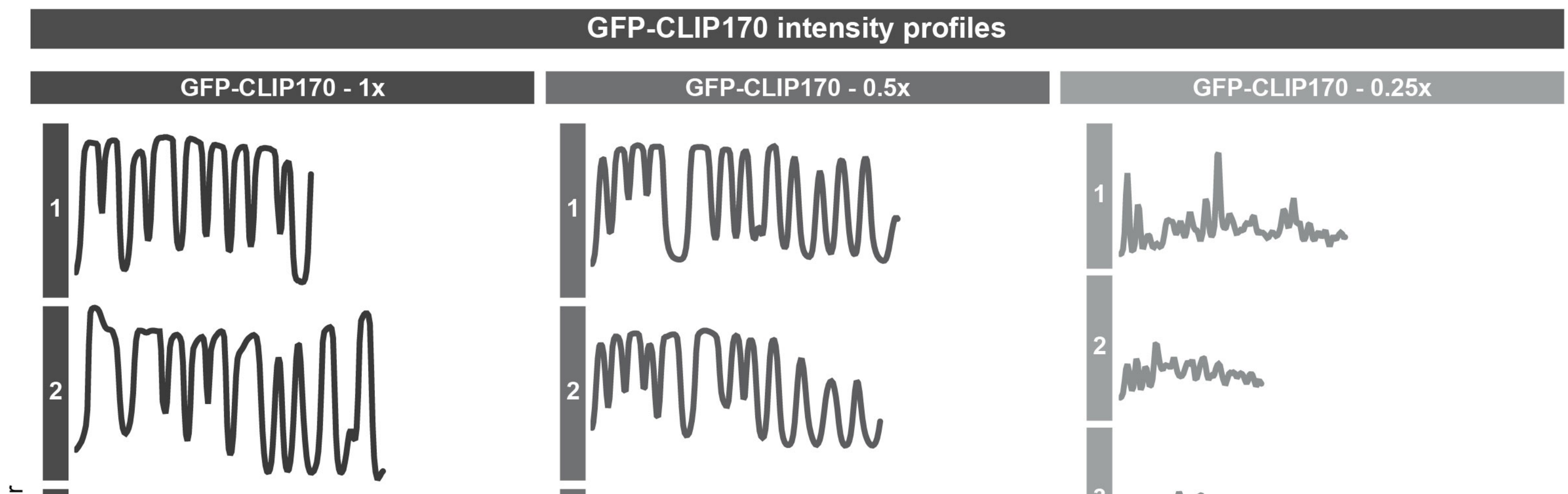

Jijumon et al. Extended Data Figure 10